INVESTIGATING CONVECTIVE CONTRIBUTION TO THE TOTAL THERMAL CONDUCTIVITY OF POROUS GLASSES FABRICATED BY ADDITIVE MANUFACTURING

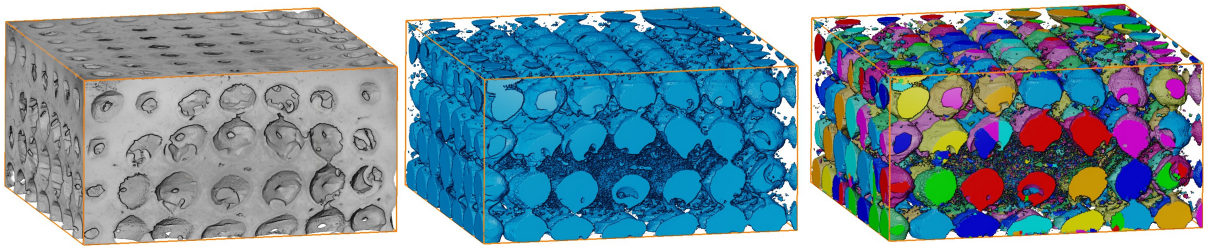

CHRISTINE BIRKEMARK PEDERSEN

MASTER THESIS

CHEMICAL ENGINEERING

AALBORG UNIVERSITY

2ND JUNE 2025

Department of Chemistry and Bioscience
Chemical Engineering
Frederik Bajers Vej 7H
9220 Aalborg Ø
www.bio.aau.dk

AALBORG UNIVERSITY

Title:

Investigating convective contribution to the total thermal conductivity of porous glasses fabricated by additive manufacturing

Project:

Master's Thesis

Project Period:

1st September 2024 – 2nd June 2025

Student:

Christine B. Pedersen

Supervisors:

Martin B. Østergaard
Bastian S. Kirkebæk

Number of Pages: 44
Appendix: 3
Finished: June 2, 2025

Preface

A prerequisite for reading the paper is the knowledge acquired from a BSc in chemical engineering and a MSc in Engineering (Chemistry) from Aalborg University. The help from the two supervisors Dr Martin B. Østergaard and Bastian S. Kirkebæk has been greatly appreciated in the making of this the thesis.

Thanks also to Dr Biao Cai and his research group at the University of Birmingham for their knowledgeable guidance and hosting me for three very special months.

Lastly, thank you to Knud Højgaards Fond and Inge Mogensens Fond for sponsoring me and making my visit at the University of Birmingham possible.

Reading guide

The references in the project are made using the Vancouver system, and appear in chronological order of use in the report. The reference is placed at the end of sentence or paragraph where it refers to the preceding piece of text. The complete bibliography can be found at the end of the report.

References to figures, tables and equations appear with chapter number followed by the reference number for the chapter. Each figure and table has a caption with additional information below or above, respectively. The figures have been made by the authors unless otherwise specified. A list of the different abbreviations used can be seen after the preface. The abbreviations are listed in alphabetical order.

Christine Birkemark Pedersen

cbpe20@student.aau.dk

Abstract

Traditional fabrication methods for porous glass structures offer limited control over pore geometry and connectivity, hindering systematic studies of heat transport mechanisms. In this work, additive manufacturing, specifically masked stereolithography, was employed to fabricate porous structures using CRT glass particles at a 50 wt.% loading. Designed macro-pores ranging from 2–7 mm were successfully produced, with X-ray tomography confirming the targeted geometry as well as revealing localized deformation, including slurry buildup, pore size reduction, and crack formation. Image-based and gravimetric porosity measurements demonstrated lower-than-designed porosity due to shrinkage during sintering and deformation. Despite these changes, the dominant presence of macro-pores and a high degree of pore connectivity were retained, as indicated by image-based pore network modeling, and most unconnected pores were localized to the struts and pore walls. Thermal conductivity simulations based on the image-based analysis showed a decrease in conductivity with increasing pore size, which aligned with experimental observations. While similar porosity levels across samples limited direct evaluation of structural influence, the results highlighted the critical role of pore geometry. Forced convection experiments further revealed that samples with larger, well-connected pores exhibited increased thermal conductivity at higher flow rates, confirming the effect of forced convection on the effective thermal conductivity. This study demonstrates the viability of AM for producing customizable porous glass structures and provides new insights into the relationship between pore structure and thermal transport in porous glass.

Resume

Traditionelle fremstillingsmetoder til porøse glasstrukturer giver begrænset kontrol over poregeometri og forbindelse, hvilket hindrer systematiske undersøgelser af varmetransportmekanismer. I dette arbejde blev additiv fremstilling, specifikt maskeret stereolitografi, anvendt til at fremstille porøse strukturer ved hjælp af CRT-glaspartikler med en mængde på 50 vægt%. Designede makroporer på 2-7 mm blev fremstillet med succes, og røntgentomografi bekræftede den målrettede geometri samt afslørede lokal deformation, herunder opbygning af slurry, reduktion af porestørrelsen og dannelse af revner. Billedbaserede og gravimetriske porøsitetsmålinger viste en lavere porøsitet end planlagt på grund af svind under sintring og deformation. På trods af disse ændringer blev den dominerende tilstedeværelse af makroporer og en høj grad af poreforbindelse bibeholdt, som det fremgår af billedbaseret porenetværksmodellering, og de fleste uforbundne porer var lokaliseret til porevæggene. Simuleringer af varmeledningsevne baseret på den billedbaserede analyse viste et fald i ledningsevne med stigende porestørrelse, hvilket stemte overens med eksperimentelle observationer. Mens lignende porøsitetsniveauer på tværs af prøverne begrænsede den direkte evaluering af strukturel indflydelse, fremhævede resultaterne poregeometriens kritiske rolle. Forsøg med tvungen konvektion afslørede desuden, at prøver med større, velforbundne porer udviste øget varmeledningsevne ved højere flow rate, hvilket bekræfter effekten af tvungen konvektion på den effektive varmeledningsevne. Denne undersøgelse viser, at AM kan bruges til at fremstille porøse glasstrukturer, der kan tilpasses, og giver ny indsigt i forholdet mellem porestruktur og varmetransport i porøst glas.

Nomenclature

List of abbreviations used throughout the thesis, in alphabetical order.

Abbreviation	**Meaning**
AM	Additive Manufacturing
CA	Compressed air
CAD	Computer Aided Design
CRT	Cathode Ray Tube
CT	X-ray Tomography
DSC	Differential scanning Calorimetry
EqD	Equivalent diameter
HEMA	2-hydroxyethyl Methacrylate
MSLA	Masked Stereolithography Apparatus
p-HEMA	Polymerized HEMA
RI	Refractive Index
TMPTA	Trimethylolpropane Triacrylate
UV	Ultra Violet
VPP	Vat Photopolymerization

List of variables and constants used throughout the thesis, in alphabetical order.

Symbol	**Unit**	**Description**
λ_e	$\mathrm{Wm^{-1}K^{-1}}$	Thermal conductivity
ρ_{air}	$\mathrm{gcm^{-3}}$	Density of air
ρ_{foam}	$\mathrm{gcm^{-3}}$	Density of porous structure
ρ_{pow}	$\mathrm{gcm^{-3}}$	Powder density of CRT panel glass
ρ_{skel}	$\mathrm{gcm^{-3}}$	Skeletal density porous structure
ρ_{water}	$\mathrm{gcm^{-3}}$	Density of demineralized water
ϕCP	(%)	Closed porosity (gravimetric)
ϕOP	(%)	Open porosity (gravimetric)
phi	(%)	Porosity (gravimetric)
k_{conv}	$\mathrm{Wm^{-1}K^{-1}}$	Thermal conductivity contribution from convection
k_{gas}	$\mathrm{Wm^{-1}K^{-1}}$	Thermal conductivity contribution from gas phase
k_{rad}	$\mathrm{Wm^{-1}K^{-1}}$	Thermal conductivity contribution from radiation
k_{solid}	$\mathrm{Wm^{-1}K^{-1}}$	Thermal conductivity contribution from solid phase
$w_{air}	(g)	Weight of porous glass in the air
$w_{water}	(g)	Weight of displaced water while porous glass is submerged
q	$\mathrm{Wm^{-2}}$	Heat flux

Contents

1 Introduction

Materials play a fundamental role in the control and management of heat in technological systems, and the selection of materials extends beyond mechanical or chemical considerations to include their thermal behavior [1]. In thermal applications, materials can be required to either promote rapid thermal transport or to serve as effective barriers to heat flow, and both ends of this spectrum are highly technologically relevant [2]. This dual functionality places thermal control at the center of material design across diverse fields, including energy conversion, thermal protection, electronics and construction [3]. Developmental efforts on producing foams with a variety of different materials have increased significantly in recent years due to their increasing applications in numerous technological fields. The unique structural properties, such as large surface area to volume ratio of the highly porous foams, makes them very useful for a wide range of industrial applications, especially where heat transfer is of primary concern [4]. Metallic foams are often utilized for their high heat transfer properties, making them ideal for applications requiring efficient heat dissipation, such as heat exchangers. On the other hand, ceramic and glass foams are utilized for their low heat transfer properties, which are useful in applications requiring heat retention or thermal shielding, such as building insulation, aerospace thermal protection systems and energy-efficient furnaces and kilns [3, 2].

Glass foam is one of the most sustainable thermal insulation materials due to its attractive insulation properties, load-bearing capability, long lifespan and potential for use of waste materials in its production. [5]. Its thermal properties depend not only on the intrinsic thermal conductivity of glass, but also critically on the material's porosity. Introducing pores will inherently reduce the heat conduction of the material, as the internal void structure, especially if tortuous, disrupts the continuity of the solid phase [6, 7]. The thermal conductivity is strongly correlated with the foam density and subsequent porosity and by tailoring porosity as well as pore size, shape, distribution, the effective thermal conductivity can be tuned over several orders of magnitude, making glass foams attractive as insulation material [8]. Current manufacturing methods for producing foam glass is sintering of powdered glass mixed with suitable foaming agents, and it is a process which can be controlled in a way that leads to a precise density and subsequent porosity. While traditional glass foam production methods enable control over density and overall porosity, they offer limited precision in tailoring pore geometry and distribution [9]. This lack of control poses challenges in systematically studying thermal transport mechanisms, especially when aiming to isolate or quantify specific contributions. As interest grows in glass foams with open or interconnected pore structures, understanding the full range of heat transfer pathways becomes increasingly important. The effective thermal conductivity is dominated by contributions from the gas and solid phases, and efforts for further minimization center around the introduction of gases with sub-air conductivity or further reducing the solid phase of the foams [9, 10]. The contribution of radiation is neglected as at ambient temperatures and convection is believed to play an insignificant role in samples with small and closed pores [5]. However, glass foams with open pore structures are increasingly being investigated, there is an increasing need to accurately understand all contributions to heat conduction

[8, 6].

Investigations into the convective contribution require a controllable pore structure, which is not currently available with traditional foaming mechanisms. In this context, advanced fabrication techniques that allow for the deliberate design and reproducible production of complex porous structures become especially valuable. Additive manufacturing (AM) has emerged as a manufacturing tool, allowing for flexible preparation of highly complex an precise structures, that are otherwise difficult to produce with traditional manufacturing methods [11]. AM covers a series of advanced manufacturing technologies used to fabricate physical parts in a layer-by-layer additive manner from three-dimensional Computer Assisted Design (CAD) models that are digitally sliced into two-dimensional cross sections. The major ways AM techniques vary are how the layers are created and how the layers bond to each other. These differences will impact factors like accuracy of the final parts in addition to the physical and mechanical properties of the final part [12]. Some common AM methods are fused deposition modeling, powder bed fusion, inkjet printing and stereolithography. Additionally, each method differs in the materials used and their application. Materials that can be used for AM include continuous filaments of thermoplastic polymers, metal and alloy powders, ceramic and concrete particles dispersed in a liquid binder and photo-active monomers [13]. In order to achieve a glass or ceramic structure with AM, slurry-based technologies can be utilized. These involve a photo-active liquid system dispersed with fine ceramic or glass particles as feedstock [11, 14]. Especially in manufacturing of complex porous tissue engineering, AM with glass particles has proved successful. Chiu et al. [15] utilized AM methods to fabricate bio-active glass scaffolds and were able to produce highly complex structures with a 42.5 wt.% particle load. Similarly, Zhang et al. [16] produced bio-ceramic scaffolds with a controllable porous structure with a 60 wt.% solid load utilized for bone reconstruction.

AM has the potential to manufacture porous glass structures, where the porosity and pore structure is controllable. Designing and printing of specific porous glass structures can help to further understand the relationship between the effective thermal conductivity and pore structure and to investigate the influence of the convective contribution.

2 Theory

2.1 Vat Photopolymerization

Vat photopolymerization (VPP) can be used as a slurry- based AM method. It uses makes use of liquid, ultra violet (UV) curable resins as the primary material. A vat containing the resin is then exposed to repeated patterns of irradiation corresponding to cross sections of the part being built [12, 17]. Masked Stereolithography Apparatus (MSLA) is a VPP derivative, where an integral image is transferred to the photopolymerizable liquid surface by exposing it to UV light through a patterned mask. With MSLA the mask is generated by a LCD screen [11, 15]. Photopolymers utilized in VPP are composed of different components, that ensure the desired polymerization. A resin could be composed of a monomer base, a cross-linker and a photoinitiator. Irradiation of the photoinitiator with UV light emitted from the LCD screen will make it reactive with the monomer base, which will start a polymer chain. Additional reactions will occur to further grow the polymer chains. The cross-linker is present to ensure the creation of strong covalent bonds between the polymer chains [12].

A slurry based MSLA process can be divided into five distinct parts; slurry preparation, printing, cleaning, debinding and sintering, resulting in the final part, as seen in Figure 2.1:

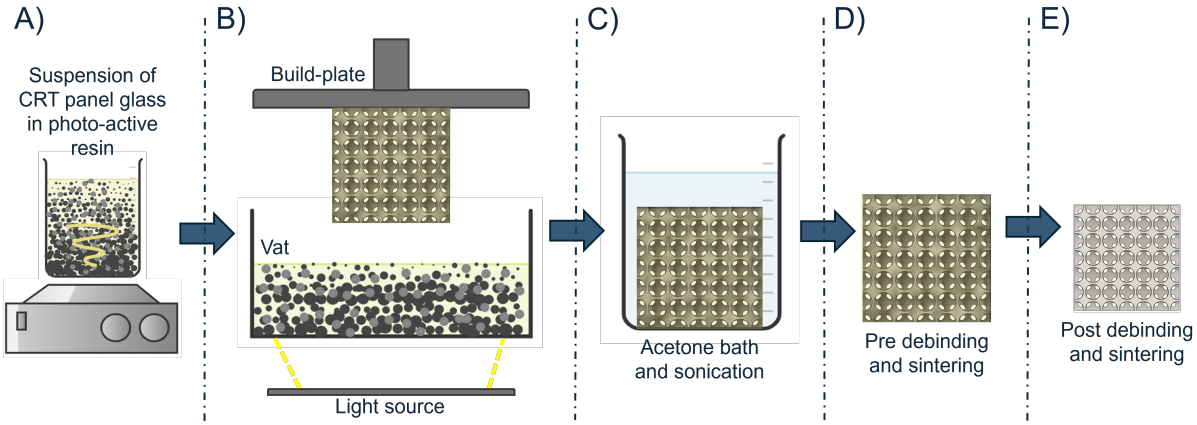

Figure 2.1: Slurry based VPP process: A) slurry preparation, B VPP, C) cleaning, D) Debinding and sintering, E) final part

The glass particles and photosensitive resin are mixed proportionally in order to prepare a glass slurry with a uniform dispersion and a set solid loading. In the printer vat, the glass slurry is irradiated with UV light, in order to cure the photosensitive resin into the desired greenbody. The part is then cleaned to remove any unwanted slurry residue from the greenbody. In order to achieve a pure-glass sample, the greenbody is heated to a debinding temperature. When the resin is removed, the greenbody in continuously heated to a sintering temperature [17].

2.2 Print defects

Glass and ceramic structures manufactured by VPP offer the advantages of high precision ($\sim$ μm), high surface quality and high density [18]. However, defects in the final part can arise during manufacturing. The defects can be divided into two types; (1) geometry-related defects: overcuring, change or disappearance of geometric features, step effect, uneven shrinkage deformation, warping, and (2) performance-related defects: cracks along the layer, cracks through the layer, uneven density, inclusions and pores, printing-related mechanical properties and intergranular cracking [17].

Understanding the origins of these defects requires examining the entire VPP process. Each processing stage, slurry preparation, printing, debinding, and sintering, can introduce specific flaws that compromise the quality and functionality of the final part.

2.2.1 Slurry preparation

In the preparation of the slurry the particle size distribution, solid content, and the corresponding sedimentation characteristics of the glass powder in the slurry, affects the subsequent printing and densification process [18]. A slurry with high solid content, low viscosity, and low sedimentation is desirable, as this allows the slurry to self-level between curing of the layers and to ensure the dispersion stability [19]. Fan et al. [20] showed that the particle size of the ceramic powder had a significant impact on the microstructure of the manufactured samples. A coarser powder resulted in a microstructure with looser particle packing and larger number of pores, as a smaller particle size enhanced the densification during sintering. The stability of the particle dispersion depends on the particle size, as smaller particles experience weaker gravitational forces and exhibit lower sedimentation rate. However, smaller particles with higher surface energy tend to aggregate, which can make it difficult to disperse the particles into the photopolymer resin [15].

Schwarzer et al. [21] investigated the impact of the viscosity of the ceramic and resin slurry on the quality of the final print. An excessively high viscosity of the slurry will affect the resolution of the printed part. A lower solid content will result in reduced viscosity, however, decreasing the solid content can increase the effects of shrinkage during subsequent thermal treatment, as a greater proportion of the printed mass is lost during debinding. It would also pose a challenge to produce sintered parts with a very high sintered density [18, 21].

2.2.2 Printing

In VPP, an UV light source is used to cure the photosensitive resin. In a homogeneous medium without particles, the attenuation of light is typically absorption-dominated. However, when a large number of particles are suspended in the resin, they act as the scattering center for the incident light, resulting in light scattering [22]. The particles increase the total refractive index (RI) of the slurry, and contribute to the refraction, blockage, and scattering the UV light. Consequently, the solid content of the slurry affects the resolution of the greenbody [18]. The curing depth during irradiation depends on the penetration of UV light into the slurry. Hereby determining the polymerized thickness of the slurry when curing of a single layer, as well as influencing the interlaminar bonding of the different layers. The curing depth can

be increased by extending the exposure time for each layer or by adjusting the slurry composition [23]. A larger layer thickness reduces printing time by reducing the total number of layers printed, a smaller layer thickness, however, makes it possible to print more delicate structures with higher accuracy [21]. The penetration depth of the slurry is influenced by different factors: size of the ceramic/glass powder, the interparticle distance (degree of dispersion, solid content), and the RI of both the ceramic powder and resin. The RI of the particles will be higher than that of the resin, and the greater difference in RI between them leads to a decrease in the penetration depth of the slurry [24]. Thus, curing of the resin can lead to defects in the greenbody in several ways. The high RI of the slurry lead to over-curing, which reduces the geometric accuracy of the final structure. Additionally, the attenuation of the irradiation at the bonding interface between two cured layers, may result in a reduction in the interlayer bonding strength. The interlayer bonding surfaces are more likely to crack under stress, and exhibit a lower elastic modulus and reduced degree of cross-linking compared to other regions in the greenbody [18].

After the manufacturing process is finished, the samples need to be removed from the build-plate. Depending of the structure of the greenbody, supports may have been required during printing and should be removed prior to debinding. The removal can be the cause of structural defects, including missing sample structure, dimensional errors and residual support material [18]. In order to minimize the difference between the CAD structure and the final sintered sample, residual slurry must be removed from the part after printing. Residual material may fill intentional voids, causing them to disappear or be blocked [18]. If the viscosity of the slurry is to high, uncured material may be unable to flow out of the pore structure or off the surfaces. Additionally, it will be less prone to dissolve and dilute in a cleaning agent [25].

The difficulty of cleaning VPP greenbodies is closely linked to the characteristic of both the slurry and the printed part. Key factors include slurry viscosity, the solubility difference between the slurry and the polymerized greenbody, shape complexity and mechanical properties of the greenbodies - all of which significantly impact the cleaning process [25]. There are many different methods used for cleaning samples produced with VPP; surface cleaning or submersion within a cleaning agent, high pressure gas, and ultrasonic treatment are some of them [18, 26, 21].

2.2.3 Debinding

During the debinding process, the polymer binding the particles together in the printed part is removed leaving only the glass or ceramic particles. The debinding can cause defects such as peeling, micro-cracks or overall cracking [18, 27]. The part is heated to a temperature causing the decomposition of the binder intro smaller molecules, which evaporates from the surface of the particles. An non-uniform permeability increases the organic vapor pressure in the printed parts and can lead to the occurrence of defects such as cracks or shape deformation. When removing the binder, the decomposed components can more easily pass through weakly connected spaces, such as the interlayer spacings [28]. Both the heating rate and the permeability of the greenbody influence defect formation. When the gas-phase product formation rate exceeds the diffusion rate, the internal gas pressure within the greenbody increases. If the decomposition rate is low delamination will happen at the interfaces, however as the rate increases the cracks will also initiate through the layers. This is particularly pronounced in parts with thick walls

and large cross-sections [18].

The high polymer content in a greenbody produced with VPP also experience shrinkage during debinding. Li et al. [28] found, that the shrinkage was the greatest in the Z direction, compared to the X-Y direction. They attributed this increased shrinkage to weaker binding to adjacent layers in the Z-direction.

The debinding atmosphere can also influence the debinding process. Li et al. [27] investigated the influence of the debinding atmosphere on the mechanical properties of ceramics produced with AM. An air atmosphere lead to a higher strength and relative densities, compared to an argon or vacuum atmosphere. However, debinding under an argon atmosphere reduces the volatilization rate of the polymer phase compared to air, thereby decreasing the likelihood of cracks and deformation of samples [28], however removing the organic binder in an inert atmosphere leaves behind a carbon residue. Mao et al. [29] used a two-step binding procedure, in which the greenbodies were first treated in an argon atmosphere to remove the polymer binder. An additional firing in an air atmosphere was used to eliminate the carbon produced by the first debinding step.

2.2.4 Sintering

Sintering of the particles of the debinding greenbody is the last crucial step in producing the final sample. After debinding no organic material should be left in the greenbody, which means nothing is binding the individual particles together and the solid phase is less dense [28]. The sintering process is the cause of all the dimensional changes to the greenbody and is crucial in order to provide the structure with both their macro- and microstructure, and corresponding structural and functional properties [30].

As a significant portion of the greenbody mass is removed during the debinding, shrinkage is expected during the sintering process. This shrinkage should be small and isotropic. However, the layer-by-layer manufacturing process leads to an anisotropic shrinkage [31]. The anisotropic nature of the sintering tends to generate distortions in the samples. Anisotropy can arise from different factors, including the particle shape, structure, and orientation, as well as particle packing, porosity, and gravity. The anisotropy originates from a gradient of microporosity between the printed layers. The Z-direction shrinks more because of pores that are more easily eliminated. In contrast, the XY-direction contains denser middle layer regions which resists shrinkage [32, 31]. However, the sintering will not completely eliminate the interlayer pores and cracks which may have been formed during debinding. The layered nature is carried over, retained and transformed during the sintering process [18].

2.3 Thermal conductivity of porous materials

Thermal conductivity is a material property that quantifies the amount of heat crossing a unit area per unit temperature gradient. The one-dimensional thermal conductivity of a material is express by Fourier's law of heat conduction, as seen in Equation 2.1:

$$q = -\lambda(dT/dz) \tag{2.1}$$

where λ is thermal conductivity of the material ($\mathrm{Wm^{-1}K^{-1}}$), dT/dz is the temperature gradient ($\mathrm{Km^{-1}}$) and q is the heat flux ($\mathrm{Wm^{-2}}$) [33].

In porous media, the thermal conductivity is influenced not only by the intrinsic properties of the constituent materials but also by the microstructure. The effective thermal conductivity can be expressed as the sum of four primary modes of heat transfer, as seen in as seen in Equation 2.2:

$$k_{eff} = k_{solid} + k_{gas} + k_{rad} + k_{conv}(Wm^{-1}K^{-1}) \tag{2.2}$$

These terms represent the contribution from solid-phase conduction (k_{solid}), gas-phase conduction (k_{gas}), thermal radiation through the pore structure (k_{rad}), and convection (k_{conv}) within the pore network. k_{eff} of a material is complex, and optimizing the insulating properties of a material might require control of each individual contribution. Reducing the density will reduce the solid cross-sectional area available for conduction while increasing the area dominated by the less conducting gas [34]. With increasing porosity, the contribution from the gas-phase conduction becomes increasingly more influential. Gases generally exhibit thermal conductivities that are orders of magnitude lower than solids due to larger intermolecular distances, and increasing the proportion of gas-filled voids as well as introducing gases with sub air thermal conductivity will reduce k_{eff} [4]. In addition to conduction, thermal radiation can also contribute to heat transfer within porous materials, particularly at elevated temperatures. It is a complex process, especially in heterogeneous materials due to the interaction of photons with the complicated pore structures and material interfaces. The contribution is mostly relevant for materials used under solar/laser heating, high temperature, and vacuum insulation materials [6]. It is however mostly neglected in porous materials utilized at ambient temperatures [5].

Convection is generally considered significant under certain conditions, particularly in materials with large or interconnected pores that enable fluid motion. In most porous materials with small, $<4\,\mathrm{mm}$, and closed pores, natural convection is suppressed due to the limited pore space [35, 5]. In such cases, k_{conv} is often excluded from the thermal models under the assumption that it does not contribute meaningly to the overall heat transfer. Zhao et al. [35] states, that the overall performance of a high conducting thermal system can be substantially enhanced by introducing pore structures designed for convective thermal transport. Open and tortuous pore structures promote flow mixing, and can increase the contribution from convection. This effect is unwanted in insulating materials, however pore structure and porosity can be complicated to control and predict [9, 36], making the contribution more difficult to completely avoid in high porosity materials.

3 | Initial work

3.1 Sample preparation

Utilizing MSLA while suspending glass particles in the resin to produce macro porous structures was an iterative process, where many variables were adjustable. The objective was to produce a glass structure with a known porosity and pore size in order to understand the influence of pore structure on k_{eff}. Pedersen et al. [37] investigated the effect of slurry composition, in order to achieve an stable suspension for printing with CRT panel glass. They concluded that an addition of 0.5 wt.% of Tween-80 was the optimal surfactant, and that a smaller particle size of CRT panel glass was ideal. These observation was the jumping off point for this project.

The initial sample preparation followed the steps seen on Figure 3.1:

Figure 3.1: Steps for 1st iteration of sample preparation.

As reported in Section 2.2.1, the composition of the slurry will affect the overall quality of the printed parts. A small particle size is significant in order to achieve a stable suspension and minimize the defects in the final sample [18, 37]. After debinding and sintering major deformation of the samples was observed. These samples had glass particles which had been disc milled for $60\,\mathrm{s}$ at $1.500\,\mathrm{rpm}$, which reduced their particle size to <63μm. However, when compared to glass particles which was not disc milled the deformation significantly reduced, as seen on Figure 3.2.

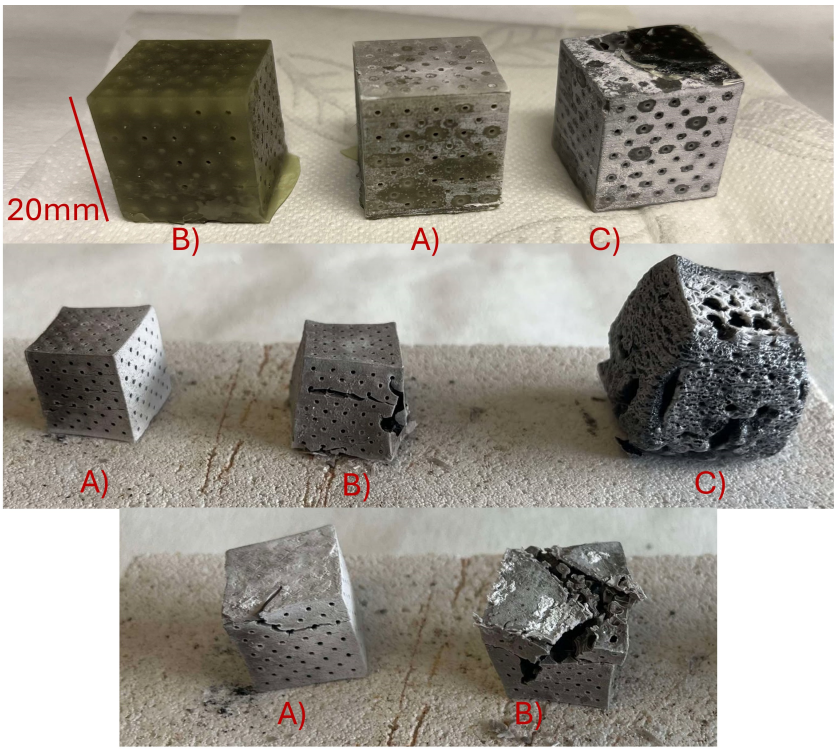

Figure 3.2: Porous CRT panel glass samples before and after heat treatment. A) sample slurry was prepared with particles untreated with disc milling, and post print the sample was treated with sonication in acetone before, B) sample slurry was prepared with particles untreated by disc milling and post print the sample was not treated with sonication in acetone, and C) sample slurry was prepared with particles treated by disc milling and post print the sample was treated with sonication in acetone.

Sample A) was printed with a slurry, where the glass particle was not treated to reduce the particle size. Post print it was submerged in acetone and subsequently subjected to sonication. Th sample experienced crack formation in the bottom, however not to the same degree as seen in Sample B). This sample was printed in the same batch as Sample A), but was not subjected to ant kind of cleaning. The sample experienced a significantly higher degree deformation, and it can be seen that the whole structure was deformed. Sample C) was printed with a slurry, where the glass particles was treated with disc milling in order to reduce the particle size below <63μm. The same cleaning procedure for Sample A) was utilized, in order to properly access the effect of reducing the glass particles. Sample C) experienced significant expansion of the whole structure, a type of deformation not observed in Sample A) or B). In order to prevent this type of deformation, reducing the particle size with a disc mill was avoided for further slurry preparation, however this could cause deformation in its own right. Reducing the amount of deformation during heat treatment can be done by introducing cleaning of the greenbodies post print. Xing et al. [38] investigated different post-processing of as-printed vat photo-polymerized polymer-derived ceramics to improve the heat treatment outcome. Ultrasonic cleaning with the help of a cleaning agent was tested as suitable cleaning method, and was found to remove uncured resin in the greenbody. As ultrasonic treatment in a bath of acetone is a simple method of cleaning, this was utilized in the preparation of the samples. This step helped remove residue of uncured resin left in the pore structure surface after printing [18]. Comparing the degree of deformation between Sample A) and B) confirms that the sonication in

an acetone bath helps reduce the amount of deformation.

3.2 Heat treatment

In order to achieve a pure glass sample heat treatment is needed to remove the photopolymerized resin and subsequently sintering of the glass particles. The temperature program for this process is based on the decomposition temperatures of the resin components and the sintering temperature of CRT panel glass, as seen in Table 3.1:

Table 3.1: Significant temperatures for heat treatment of the greenbodies.

	P-HEMA [39]	**TMPTA [40]**	**Irgacure 819 [41]**	**CRT panel glass [42]**
Approx. decomposition (°C)	299	~380	~590	-
Sintering (°C)	-	-	-	~700

Some of these temperatures are approximate decomposition temperatures, as they are derived from the boiling point of TMPTA and Irgacure-819 [40, 41]. Pedersen et al. [37] performed a differential scanning calorimetry (DSC) analysis, in order to further investigate the thermal properties of the cured photopolymer. This analysis was done on the pure resin, i.e. without the presence of glass particles, as seen on Figure 3.3:

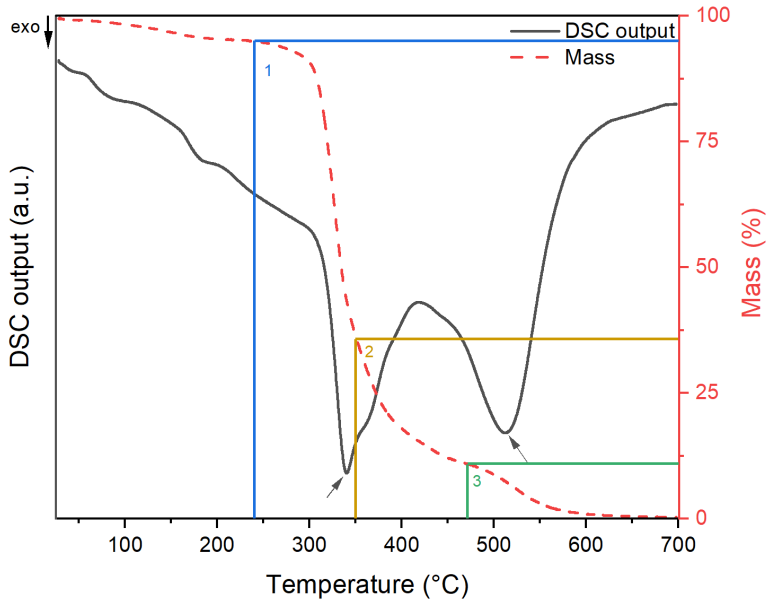

Figure 3.3: DSC analyses of polymerized printer resin without the presence of CRT panel glass. Exothermic peaks are highlighted by arrows, mass loss is indicated by the colored lines and numbers indicate three independent regions with mass loss [37].

An exothermic reaction is observed from ≈300°C-≈425°C and ≈425°C-≈600°C. The first mass loss is

largest and corresponds to the decomposition temperature of polymerized HEMA (p-HEMA) at 299°C [39]. This mass loss is rapid and accounts for the majority of lost mass. The second mass loss has a slower rate, and could correspond to the decomposition of the remaining p-HEMA and the boiling point of TMPTA [40]. Lastly, the third mass loss is thought to be the evaporation of some remaining TMPTA and the boiling pint of Irgacure-819 [41]. Strategic isothermal periods and a low heating rate aids in controlling the decomposition rate of the organic resin, as ensuring a low organic vapor pressure inside the part will lower the amount of deformation [28]. The key temperatures derived from the DSC analysis was used to determine where isothermal periods in the firing program should be placed.

The aforementioned observations resulted in the second iteration of samples preparation. Reducing the particle size was mitigated in order to avoid expansion during heat treatment and all samples was treated with sonication in acetone bath, in order to remove unwanted uncured slurry. The steps seen in Figure 3.4 was then reconsidered, and the final sample preparation is seen on Figure 3.4:

Figure 3.4: Steps for 2nd iteration of sample preparation.

4 | Methodology

4.1 Sample preparation

4.1.1 Resin composition

The resin composition of all slurrys was the same. The resin consisted of a standard monomer solution of 80 wt.% HEMA (2-Hydroxyethyl Methacrylate) ($C_6H_{10}O_3$, 97%, stabilized, CAS: 868-77-9) and 20 wt.% TMPTA (trimethylolpropane triacrylate) ($C_{15}H_{20}O_6$), $\geq$ 75%, stabilized with MEHQ ((4-methoxyphenol), CAS: 15625-89-5). To this standard monomer solution 5 wt.% Irgacure 819 ($C_{26}H_{27}O_3P$) was added. In order to better ensure a stable suspension, 0.5 wt.% was added to the resin. This solution was used to create a slurry with a 50 wt.% load of pulverized CRT panel glass (<63μm).

4.1.2 Print of greenbody

An Anycubic Photon Mono 2 was used to print the greenbodies from the slurry. The printer settings was 12 seconds exposure time, 1 second off time, 25 seconds exposure time for bottom layers, 5 bottom layers and a layer height of 0.1mm. Before printing the actual greenbodies, a 0.25mm raft of resin without particles was printed on the build-plate. Printed samples varied in overall size, pore size and structure. Some CAD files can be seen on Figure 4.1:

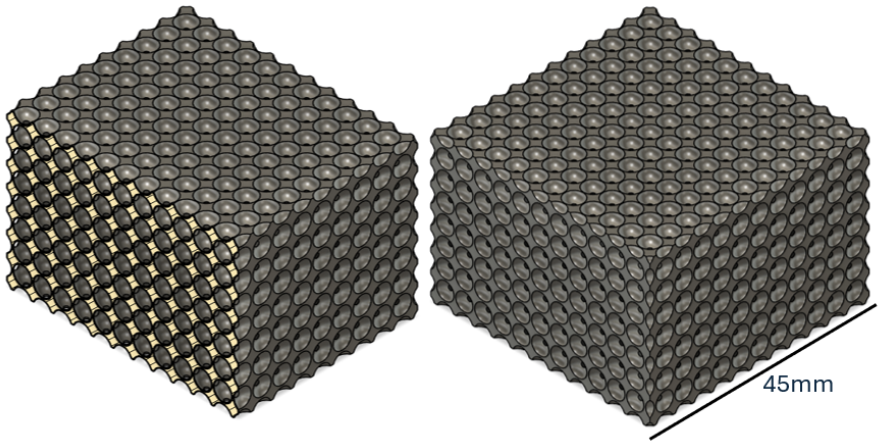

Figure 4.1: CAD file showing structure with 4mm interconnected spherical pores

The final samples is designed with an interconnected, grid pore structure, where the overlap of each pore is ~0.05mm The CAD pore size ranged from 2 mm to 8 mm.

4.1.3 Firing

Debinding and sintering of the greenbodies was carried out in one continuous firing in a tube furnace. The whole process had a $5\,\mathrm{L/min}$ flow of compressed air (CA) to ensure complete decomposition of the resin binder. Heating rate of the firing was $1\,\mathrm{K/min}$, and after sintering the cooling rate was $10\,\mathrm{K/min}$. The samples was places inside a stainless steel cylinder to ensure an even temperature around the whole sample, even with the gas flow. To allow for decomposing resin to escape the samples from the bottom, the samples was placed on top of alumina fibers. Additionally, two samples both with a CAD pore diameter of 6mm was fired sitting on a stainless steel or a ceramic plate. Debinding of the resin was done with isothermal periods of $15\,\mathrm{min}$ at 250°C and 475°C and of $60\,\mathrm{min}$ at 350°C. The temperatures corresponds with crucial decomposition temperatures of the resin components [39, 40, 41]. Sintering was done at 750 °C for $90\,\mathrm{min}$ [42]. The whole temperature program can be seen on Figure 4.2:

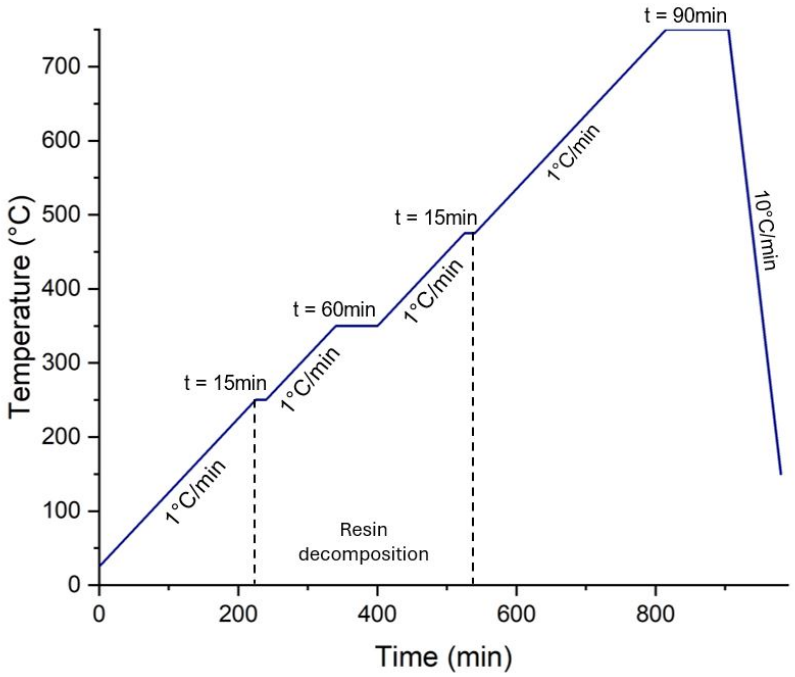

Figure 4.2: Heating program for the final samples

Sample set-up

In order to avoid the samples sintering onto the ceramic carrier plate during firing, different materials have been tested as separation material. Both a thin slice of stainless steel, a smooth ceramic plate and alumina fibers have been placed between the samples and the ceramic carrier plate. Additionally a stainless cylinder is placed around the sample to reduce the potential temperature gradient in the sample caused by the flow of air during firing, as can be seen on Figure 4.3:

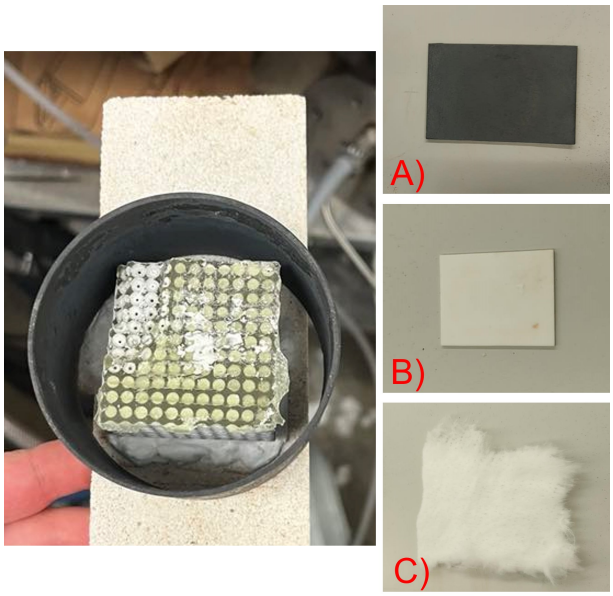

Figure 4.3: Sample set-up during firing; A) stainless steel, B) smooth ceramic and C) alumina fibers

4.1.4 Sample ID

The six final samples produces is categorized by their CAD pore size and the method of which they are fired with, as can be seen in Table 4.1:

Table 4.1: Sample ID for the six final samples.

Sample ID	CAD4	CAD5	CAD6	CAD7	F1CAD6	F2CAD6
CAD pore size	4mm	5mm	6mm	7mm	6mm	6mm
Firering set-up	Alumina fibers	Alumina fibers	Alumina fibers	Alumina fiber	Stainless steel plate	Ceramic plate

4.2 Sample characterization

4.2.1 X-ray tomography

For imaging and characterizing the internal features of the sample X-ray computed tomography (CT) was utilized. The Nikon Micro-CT XTH225 system was employed the specific scanning parameters for CAD5 were set as seen in Table 4.2. The scan settings is equal for all scan, however voxel size and count for each sample can be seen in Appendix A.1.

Table 4.2: X-ray tomography scanning parameters for CAD5.

Parameter	Value
X-ray Voltage (kV)	200
X-ray Current (μA)	50
Source to object distance (mm)	136.1
Source to detector distance (mm)	983.4
Voxel size (μm)	17.57 (X, Y, Z)
Voxel count	3192 (X), 3192 (Y), 2296 (Z)
Number of projections	2400
Initial agle	0°
Angular step	0.15°

The radiographs is utilized to reconstruct the structure of the porous glass structures, and the images are processed and analysed using Avizo 2019 (TheroFisher Scientific, Waltman, MA, USA). All samples are analysed with the same steps, and the steps of the image-based analysis can be seen in Table 4.3:

Table 4.3: Computational steps for the image-based analysis characterizing the pore structure of each sample.

Characterization of pore structure	Purpose
Resample transformed image	Reorienting of image with the global XYZ-axises.
Median filer (x3)	Removal of noice.
Interactive thresholding	Binarization of images into either solid or void. Manually set threshold.
Separate objects	Separation of open and interconnected pores into isolated pores.
Label analysis	Assigning of unique label to each pore enabeling pore structure characterization.

The image-based analysis is utilized to characterize the pore structure; determination of void volume fraction of the total volume and quantification of the pore size distribution of the separated and labeled pores. All steps allows for an qualitative analysis of the samples, as each computational step display the pore structure in different ways. For each step both 2D and 3D orthogonal slices and 3D volume renderings is utilized to properly understand the pore structure.

In order to evaluate the connectivity of the pore structure a pore network analysis is carried out the the image-based analysis, and the computational steps can be seen in Table 4.4:

Table 4.4: Computational steps for the pore network analysis quantifying and visualizing the pore connectivity of each sample.

Pore network analysis	**Purpose**
Interactive thresholding	Binarization of images into solid or void. Manually set threshold.
Axis connectivity	Determination of connected porosity
Separate objects	Separation of open and interconnected pores into isolated pores.
Generate pore network model	Modeling ot the network of connected pores. Visualization of pores and throats with spheres and cylinders.

Lastly, the image-based analysis is utilized to carry out a thermal conductivity simulation on a volume of each sample. A region of interest of ∼15x15x15mm is defined for each sample, in order to carry out the simulation, and the computational steps can be seen in Table 4.5:

Table 4.5: Computational steps for the thermal conductivity simulation for each sample.

XLab Thermal conductivity simulation	**Purpose**
Thermal conductivity experiment simulation	Simulation of the thermal conductivity
Thermal conductivity tensor calculation	Extra relavant information about the simulation.

In order to carry out the simulation the thermal conductivity of the solid- and the void-phased is defined as $0.97\mathrm{Wm^{-1}K^{-1}}$ and $0.026\mathrm{Wm^{-1}K^{-1}}$ respectively [5].

4.2.2 Density and porosity

The density of the porous glass strutures is determined based on the skeletal (ρ_{skel}) and foam (ρ_{foam}) density [9]. Ultrapyc 1200e Quantachrime Helium Pycnometer was utilized for determining the density of the skeleton based on a average value from five measurements of the volume and density of the samples. The foam density is determined through Archimedes's principle of displaced liquid due to the complex structure [43]. Demineralize water is used a the immersion liquid and the temperature was measured to be 21.7°C. The foam density calculation can be seen in Equation 4.1:

$$\rho_{foam} = \frac{w_{foam}}{w_{water}} \cdot (\rho_{water} - \rho_{air}) + \rho_{air} \tag{4.1}$$

Where w_{dry} is the dry sample weight in air (g), w_{water} is the weight of the displaced water when the sample is submerged (g), and $\rho water$ is the density of demineralized water ($\mathrm{gcm^{-3}}$) at the measuring temperature [44]. The total gravimetric porosity (ϕ) is calculated by using Equation 4.2:

$$\phi = (1 - \frac{\rho_{foam}}{\rho_{pow}}) \cdot 100 \tag{4.2}$$

where ρ_{pow} is the powder density of CRT panel glass [45]. The open and closed porosity of the total

gravimetric porosity is calculated using Equations 4.3 and 4.4:

$$\phi_{CP} = (\frac{\rho_{skel}^{-1} - \rho_{pow}^{-1}}{\rho_{foam}^{-1} - \rho_{pow}^{-1}}) \tag{4.3}$$

$$\phi_{OP} = 100 - \phi_{CP} \tag{4.4}$$

4.2.3 Thermal conductivity

The thermal conductivity of the porous glass samples is measured using a TPS2500s Hot Disk with a 5501 sensor (Kapton, radius 6.403mm) and a WKL 100 Weiss climate chamber to ensure a constant surrounding temperature of 25°C. The analysis is anisotropic, with a layer of nonconducting polystyrene. The analysing parameters was $35\,\mathrm{mW}$ and $40\,\mathrm{s}$ and the probing depth was set to $8\,\mathrm{mm}$ for all measurements. Each measurement was repeated 5 times with a 10 min holding period between each to allow for the temperature in the samples to equalize.

The influence of forced convection on the thermal conductivity was measured by placing samples in a cell allowing for uniaxial gas flow of 99.7% N_2. Three out of the six sides of the samples was covered to only allow convection in one direction, and the cell sides was packed with alumina fibers to avoid gas flow around the sample. Measurements is taken at five flow rates between $0\,\mathrm{Lmin}^{-1}$ and $2\,\mathrm{Lmin}^{-1}$.

5 | Results and discussion

5.1 Preparation of porous glass structures

Pore sizes from 2-8mm were designed and attempted to be manufactured. Both pore structures with a simple grid structure and more complex designs with smaller pores in the struts were designed. Some of the different structures can be seen in Figure 5.1:

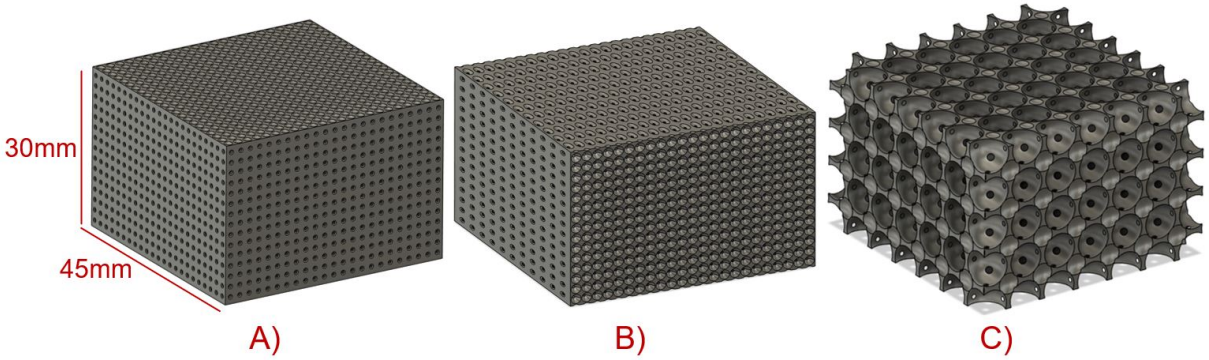

Figure 5.1: CAD files of 45mm x 45mm x 30mm porous structure. A) structure with a grid of 2mm pores, B) structure with elliptical 4mm long pores and C) structure with a grid of 7mm pores with 4.5mm pores in the struts. All pore structures are interconnected.

However, not all structures were suitable for printing, as several of the different designs experienced continued print failure. A significant cause of print failure is the force needed to separate the cured layer from the vat film, which, if high, might separate the newly cured layer from the rest of the sample. Lack of adhesion to the previous layer could be both complete or partial, and would subsequently not allow for any new layers to adhere to the already printed sample. Adhesion to the vat can be reduced by reducing the viscosity of the photo-active resin, however this becomes challenging in an already highly viscous glass or ceramic slurry [46]. Additionally, a porous geometry in the printed layer can further complicate the separation of the layer from the vat film. The force of separation increases with increasing porosity of the print geometry given the same overall printing area. The relationship between the porosity and separation force is complicated and may also depend on the shape of the previous layers [47]. Examples of samples experiencing print failure can be seen in Figure 5.2:

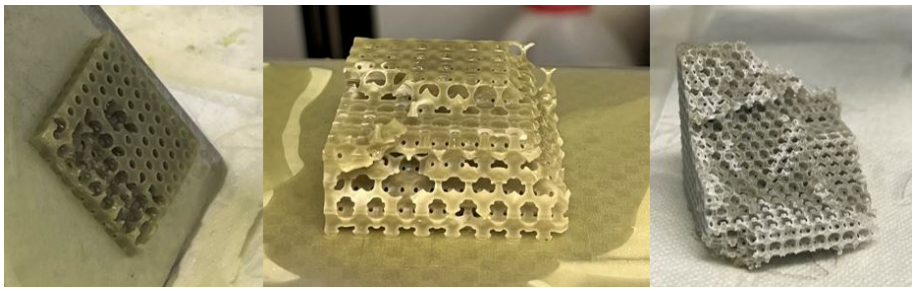

Figure 5.2: Examples of print failure. Complete or partial adhesion between the curing layer and the previous layer.

All three samples show signs of partial print failure, where the just cured layer was not able to properly adhere to the previous layer across the whole area. The print failure may happen gradually, and at layers with a high degree of void presence in the previous layers which leaves a smaller area for the new layer to adhere to. Even if it is possible cure some part of the new layers the area will remain lesser than that of the intended layer.

In the desired pore size range of 2-8mm only samples with pores in the range of 4-7mm were reasonably achieved. The final samples produced can be seen in Figure 5.3:

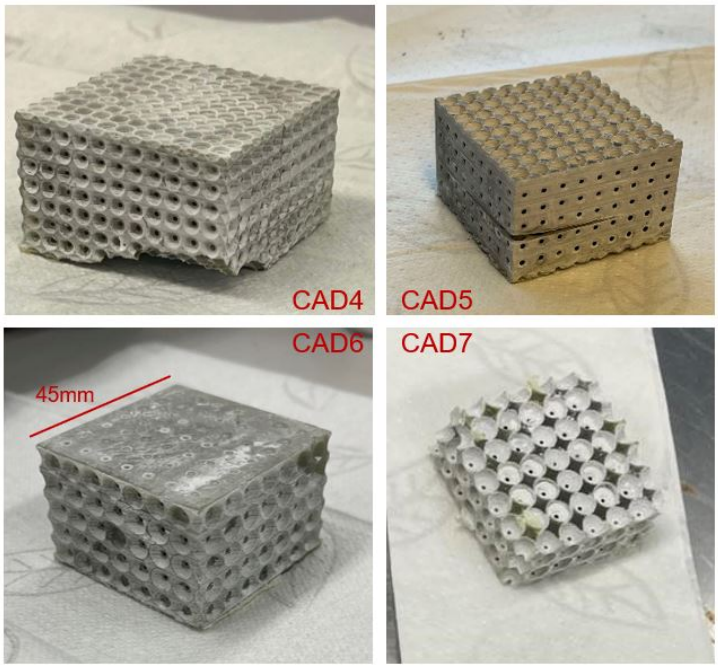

Figure 5.3: Structure of CAD4-CAD7 post printing. Structural deformation is evident in all samples, stemming from the print and subsequent demounting process.

The produced samples have a simple grid structure, without any smaller pores in the struts. The actual pore size in the structures may not be equal to the CAD pore size as producing samples with MSLA and a glass slurry has the potential for defect formation as well as a change in structure and dimension after firing. Inspecting the overall structure of the printed samples reveals structural deformation. The deformation stems from demounting from the build-plate and both partial and complete layer failure, all

defect commonly found in ceramic and glass slurry AM methods [18, 17].

5.1.1 Firing

In order to avoid adhesion to the porous ceramic plate holding the sample in the furnace during sintering, different materials was tested out. The different materials tested included a metal plate, a smooth ceramic plate and alumina fibers. The outcome of the different firing set-ups can be seen in Figure 5.4:

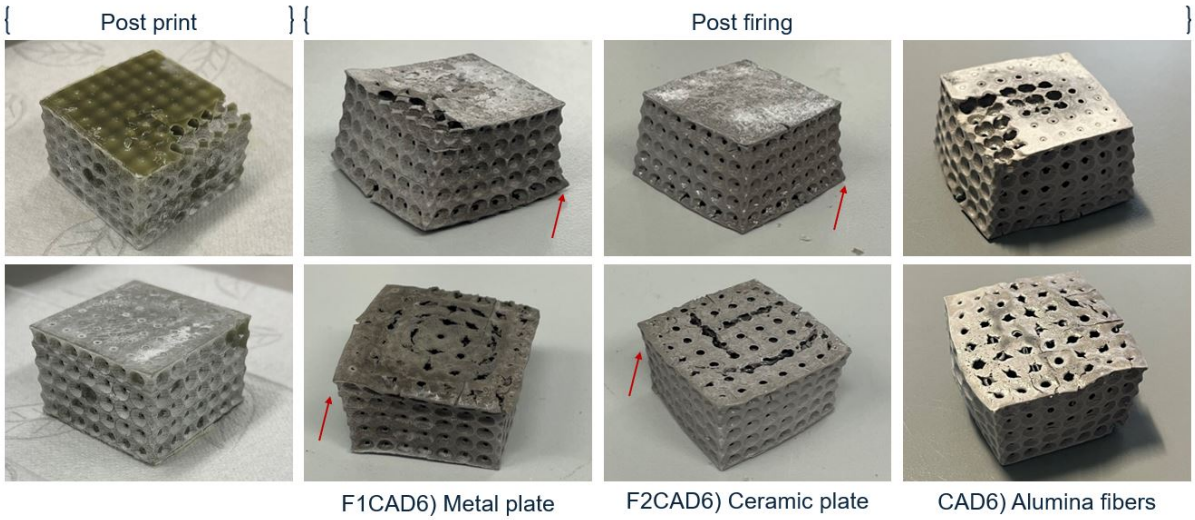

Figure 5.4: Samples post print and post firing. F1CAD6, F2CAD6 and CAD6 all had a CAD pore size of 6 mm, but had different material separating them from the ceramic carrier plate in the tube furnace. Arrows indicate areas with anisotropic shrinkage.

Firing with both the thin metal and ceramic plate led to anisotropic shrinkage in the layers in the Z-directions, where small lips were formed on the bottom edge, as indicated by the arrows. It was theorized, that this deformation occurred as the plate hindered isotropic shrinkage. Firing with alumina as the support minimized this deformation, even though some anisotropic shrinkage Z-direction was still present. The alumina fibers were subsequently used for the rest of the samples.

Between the three samples it can be seen, that F2CAD6 experienced major crack formation on the bottom compared to the other two, even with the same temperature program and CAD files. All three samples had their top layers be almost completely pore wall, however F1CAD6 is the only sample with no demounting deformation. A defect in the overall structure exposes more of the connected pore structure to the surroundings, and may help the decomposing photopolymer to better diffuse out of the sample. Without this structural deformation F1CAD6 might have experienced too high organic vapor pressure, which was equalized by major crack formation instead [28], highlighting how structure and high particle load affects the debinding process.

In Figure 5.3 the samples after printing is shown. All were fired with the same temperature program, decribed in Section 4.2. Each sample exhibit new deformation, in addition to the the deformation experienced post-print. All samples are experiencing anisotropic shrinkage mostly in the Z-direction, as there is a difference in layer surface area between the top and bottom, resulting in slightly tapered

structure. Additionally, an expansion of the overall structure has taken place, most noticeable in CAD5. CAD7 exhibits the least amount of deformation, however it also has smaller sample dimensions in the Z-direction, making it less prone deformation during firing [48].

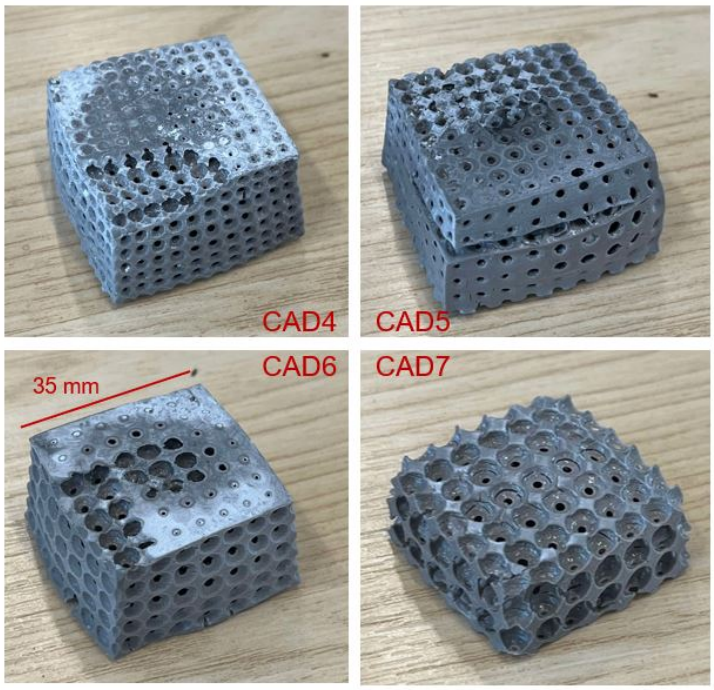

Figure 5.5: CAD4-CAD7 post firing. Structural deformation form post print is still present, as well anisotropic shrinkage from debinding and sintering.

5.2 Image analysis

X-ray tomography is a widely used technology for characterizing the internal morphology and defects in AM as it is a non-destructive method for providing both 3D visualization and a quantitative analysis of a structure [17]. The CT images are the prerequisite for the image-based analysis, and for porous materials it enables a binarization of the whole material into a solid phase and a void phase, as can be seen in Figure 5.6:

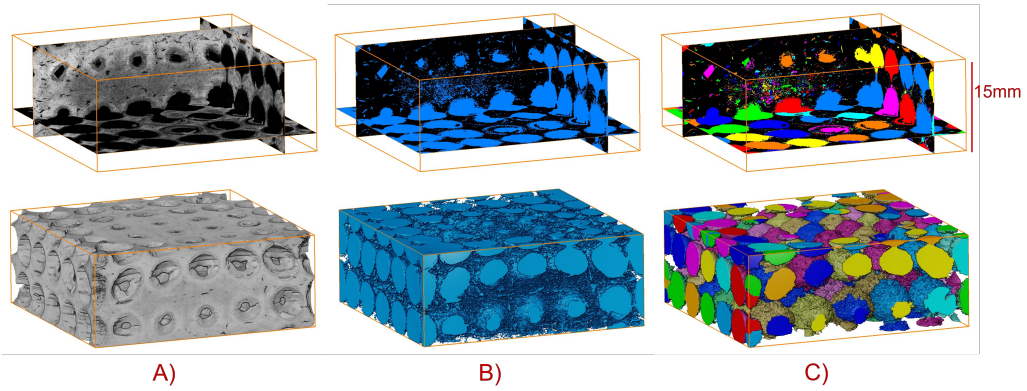

Figure 5.6: 3D orthogonal slices and 3D volume rendering of; A) CT images, B) binarization of solid- and void-phases and C) separation and labeling of each isolated pore.

While the binarized and labeled images allow for a quantitative investigation of the samples, the CT images provide a qualitative insight into the internal pore structure. 2D CT images can be utilized for observing intricate details in the structure and understanding how the pore structure behaves in different directional planes. 2D images in the XY, XZ and YZ plane can be seen in Figure 5.7:

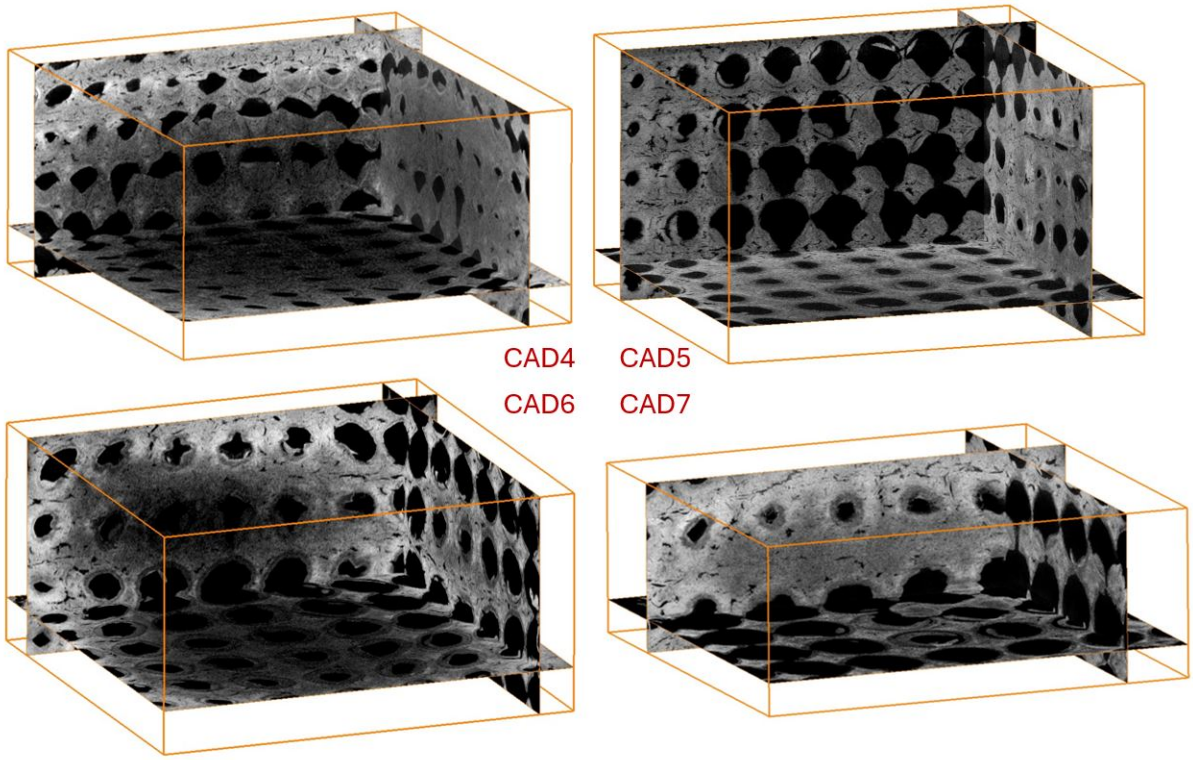

Figure 5.7: 3D orthogonal slices for CAD4-CAD7.

For all four samples, clear defects can be observed in the structure, as most pores are no longer spherical and the pore walls and struts have experienced cracking and pore formation. The solid phase in the CT images appears in a grayscale, where the color gradient displays changes in the density of the solid phase. The darker center of especially CAD4 and CAD6 indicates a degree of pore formation, most likely during the debinding process. If the organic resin is decomposed with a to high heating rate, the gases may cause the solid phase to expand or even crack [18]. This is more likely to happen in the sample center, where the distance for diffusion is the highest, resulting in a less dense solid phase. The diffusion of the resin may be further hindered by the slurry build-up on the internal surface of the macro pores, as this can block the pore throats, which would have allowed for an easier diffusion out of the structure. Furthermore, many cracks can be observed in the pore walls, especially in the layer direction. The cracks may start in the interface between two print layers and crack propagation can then migrate further into the surrounding layers if the diffusion rate is too high [28]. Furthermore the CT image reveals a density gradient across the sample. In the outer perimeter of the sample, the pore walls and struts are lighter in color and thinner. In Figure 5.5 some samples exhibit an outwards deformation resembling an expansion possibly caused by gas formation. This seems to be further supported by the CT images, where the structure of the big pores seems to be pushed outwards towards the sample edges. This is likely the result of gas evolution during debinding or sintering, leading to an expansion. Greater sample dimensions and thick pore walls

prohibit proper diffusion, which is further enhanced with a too high rate of decomposition [48].

The most critical defect in all four samples is the slurry build-up on the pore surfaces. Figure 5.8 displays a slice in the XY-direction of CAD5 and CAD7 respectively, thereby showing a cross section of the pore structure perpendicular to the print layers.

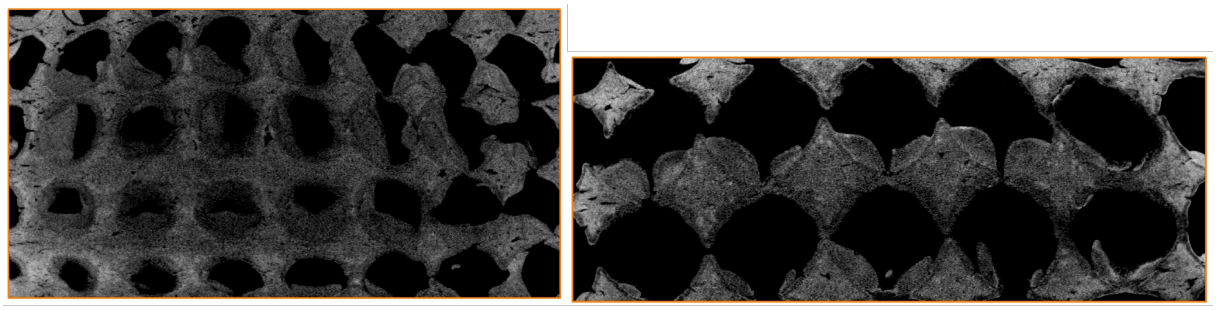

Figure 5.8: Orthogonal slices in XZ-direction of CAD5 and CAD7.

In the pores of both samples it is evident, that a significant fraction of the designed pore volume is occupied by solid. Slurry residue in the internal pore structure is common for slurry-based AM, and is usually a result of partial curing caused by light scattering or encapsulation of slurry in the pores caused by low flowability [22, 18]. In the CT images the build-up can be distinguished from the pore walls, as it appears less dense than the pore walls. Cleaning the greenbodies post printing may have effectively removed the uncured resin on the internal pore surfaces, but small pore throats and a high degree of build-up make it difficult to remove the glass particles. These are then left in the pore structure to sinter and become a part of the solid phase. In Figure 5.7 it is evident, that this deformation is taking place in all samples regardless of CAD pore size, however the closer comparison of CAD5 and CAD7 illuminates how, the build-up is more present in low pore size samples.

MSLA is a bottom-up manufacturing method, where the first layer printed belongs to the bottom of the sample. This print method utilizes the gravitational forces to help the uncured resin flow off the printed part during pauses between prints. In both CAD5 and CAD7 the build-up in some pores can be seen to primarily occupy the bottom part of the pore, indicating that the flow off the pore surface happened at a too low rate, trapping it inside the pore when additional layers were added [17]. Xing et al. [38] reported, that a reduced slurry viscosity proved effective in enhancing the flowability of the uncured slurry attached to the surface of the as-printed greenbodies with complex architectures. However, low viscosity slurries are often associated with low particle load, which in turn introduces defects such as high and anisotropic shrinkage, a less dense solid phase and lower mechanical strength [49].

5.3 Characterization of pore structure

X-ray tomography provides a quantitative analysis, based on the acquired CT images, where the binarized images are subjected to a separation step isolating the pores in order to attach a unique label to each, as seen in a slice of CAD6 in the XT-direction in Figure 5.9:

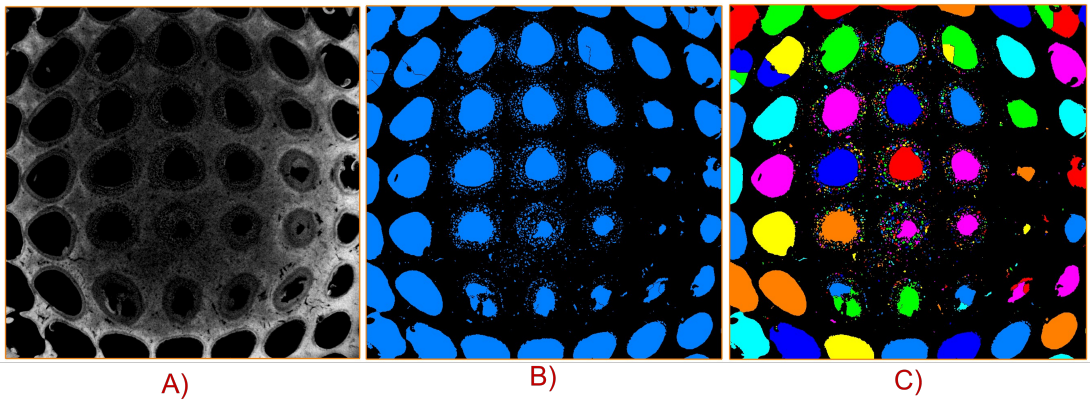

Figure 5.9: Orthogonal slices in the XY-direction; A) CT image, B) binarized solid- and void-phases and separation of pore and C) labeling of each isolated pore.

In 5.9C) the labeling of each pore is visualized with the different colors representing a separate pore volume. Some pores are seen to be divided into two or more separate pore volumes even though they appear as one pore in 5.9A). This highlights an issue with the separation step of the image analysis; wrongful separation of bigger pores [50]. In a supposedly connected pore structure however, it is a necessary step in order properly isolate each pore to characterize the pore structure [51].

5.3.1 Porosity

Binarization and separation of the voids allows for determination of the volume fraction of the total sample volume. Similarly the CAD files can be utilized to determine the porosity of the sample post printing, as they provide the intended volume of the printed greenbody. The porosity is expected to decrease during the manufacturing process, mostly due to shrinkage and possible deformation. In order to asses this, the porosity was determined from both the CAD files, with the image-based analysis and an gravimetric approach. All three porosities can be seen in Table 5.1:

Table 5.1: CAD, image-based and gravimetric porosity for all samples.

	CAD4	CAD5	CAD6	CAD7	F1CAD6	F1CAD6
CAD (%)	53,7	54,5	50,9	58,1	50,9	50,9
Image-based (%)	14,9	26,6	30,6	34,1	36,7	32,9
Gravimetric (%)	41,5	39,6	40,2	48,0	19,8	40,1

The porosities are significantly smaller than that of the initial design, most likely caused by both the inherent shrinkage of the structure during sintering and build up of slurry in the pores during printing [20, 21]. Both of these will reduce the void volume, making the porosity lower after firing, which is reflected in the gravimetric porosity. It is expected that the a image-based porosity is lower than the actual porosity, as the relatively large sample size will result in a high voxel size and the image processing, such as filtering, might conceal small pores [9]. Pores smaller than the voxel size and voxels containing multiple phases may reduce the amount of porosity detected. These limitations in the image-based analysis are more prominent when quantifying microporosity. Setting the threshold for separation of solid- and void-phases can be difficult to do accurately. Adjusting the threshold to a single layer may

lead to both under- and overestimation in different layers, as difference density and resolution might change. As the resulting solid/void ratio determines the porosity, thresholding can exclude faint or low-contrast pores as well as subtle or interconnected porosity [52, 53]. Generally, the gravimetric porosity lies between the CAD and the image-based porosity, which is to be expected. The CAD porosity only takes into account the designed pore structure and assumes a completely dense solid phase, while the image-based method might exclude some microporosity. The gravimetric porosity is in part based on the skeletal density, which is able to account for the whole pore structure. CAD4 exhibits a low image-based porosity compared to the others. This could indicate a high degree of micro pores which the image analysis is not able to properly quantify. It should be able to detect the macro pores, and the significant difference in the porosity suggests that the macro pores make up a lesser degree of the total pore volume. This might stem from a loss of pore size during both printing and firing, which is less prevalent in the samples with a greater CAD pore size. F1CAD6 is the only sample where the gravimetric porosity is lower than both the CAD and the image-based porosity, even though it has similar overall dimensions and weight as the others, it does however have a significantly higher density, as can be seen in Appendix B. The higher skeletal density suggests a low amount of micro porosity.

Determination of the gravimetric porosity allowed for calculation of the open and closed porosity. These reflect how much of the total porosity is either open or closed, and can be seen in Table 5.2:

Table 5.2: Open and closed porosity of the total gravimetric porosity for all samples.

	CAD4	CAD5	CAD6	CAD7	F1CAD6	F2CAD6
CP (%)	95.8	83.4	95.4	35.6	35.6	96.9
OP (%)	4.2	16.6	4.6	64.4	64.4	3.1

All samples were designed with a completely open and interconnected pore structure, however it can be seen that most samples exhibit a high degree of closed porosity. The loss of open porosity suggests, that the pore throats have become smaller or have closes up. It might also be a product of how the pore structure is layered. In Figure 5.5 it can be seen, that CAD7 has big and open pores compared to the other samples. Additionally, it does not exhibit the same height as the others. With a smaller distance to the center of the pore structure and the biggest CAD pore size, the conditions for an open pore structure are better. F1CAD6 similarly has a lower degree of closed porosity. The higher density of this sample indicates a more dense solid phase and less deformation in the form of expansion caused by pore generation, which may have left a higher degree of pore throats open.

5.3.2 Pore size distribution

In order to understand how the porosity is distributed, the labeling and quantification of each pore were utilized to determine the equivalent pore diameter (EqD) and pore volume, as can be seen in Figures 5.10 and 5.11:

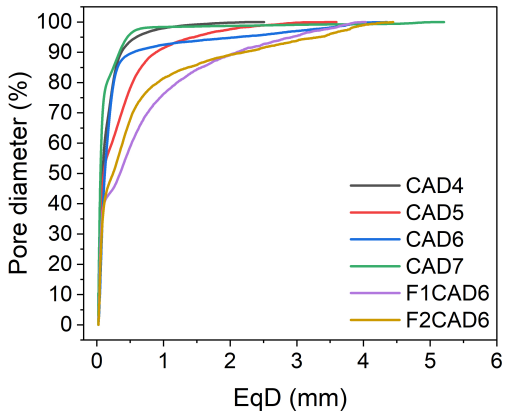

Figure 5.10: Cumulative EqD.

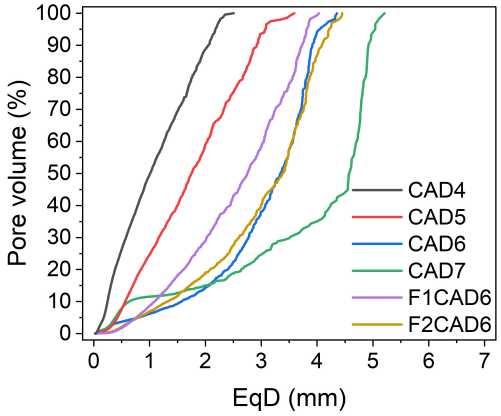

Figure 5.11: Cumulative pore volume.

The cumulative EqD distribution displays how the majority of pores in all samples are <0.5mm. CAD4, CAD6 and CAD7 exhibit a steep rise and reach 90% at lower EqD values, which indicates a pore distribution dominated by sub-millimeter pores. Both CAD6 and CAD7 reach EqD values above 4 mm, indicating that some of the pores in the samples retain a relatively big pore size despite deformation and shrinkage. F1CAD6, F2CAD6 and CAD5 exhibit more gradual increases, suggesting a broader pore size distribution. Figure 5.11 reflects the pore volume distribution across different pore sizes. Generally, the samples with a lower CAD pore size show a steeper increase, indicating that most of their pore volume is contributed by smaller pores. The increase becomes less steep with increasing CAD pore size, as their pores constitute a higher portion of the total volume. This highlights that even if a high amount of the total pore diameter can be attributed to small pores, they do not play the most significant role in the porosity. Furthermore, the gradual increase indicates a broad pore size distribution. The presence of 2-3mm EqD pores in even CAD6 and CAD7 illustrates how some pores might have been more exposed to slurry build-up and anisotropic shrinkage. It is, however, evident that this broad pore size distribution is less present in CAD7, as ∼65% of the pore volume is inhibited by >4.5mm EqD pores. The three CAD6 samples somewhat follow the same pore volume distribution. CAD6 and F2CAD6 are more aligned while also exhibiting almost equal image-based and gravimetric porosities. F1CAD6 had a significantly lower gravimetric porosity and the pore volume distribution is also less aligned, despite having the same CAD file and manufacturing method.

Both Figure 5.10 and 5.11 show that none of the samples retain the pore diameter from the CAD files. At least 1 mm is lost due to shrinkage and slurry build up in the pores during printing. Evans et al. [54] and Sajadi et al. [55] reported shrinkage in the order of ∼8-29% for ceramic structures produced with AM. The nature and the degree of shrinkage depend on both particle size, particle load in the slurry, sintering temperature and duration and the overall geometry of the parts. It is expected for sintered parts as well as samples produced by AM to experience shrinkage [20].

None of the sub-millimeter pores are included in the initial CAD files, and are subsequently formed sometime during manufacturing. The labeling of the pores allows for filtering by volume, making it possible to observe the placement of the small pores, as seen in Figure 5.12:

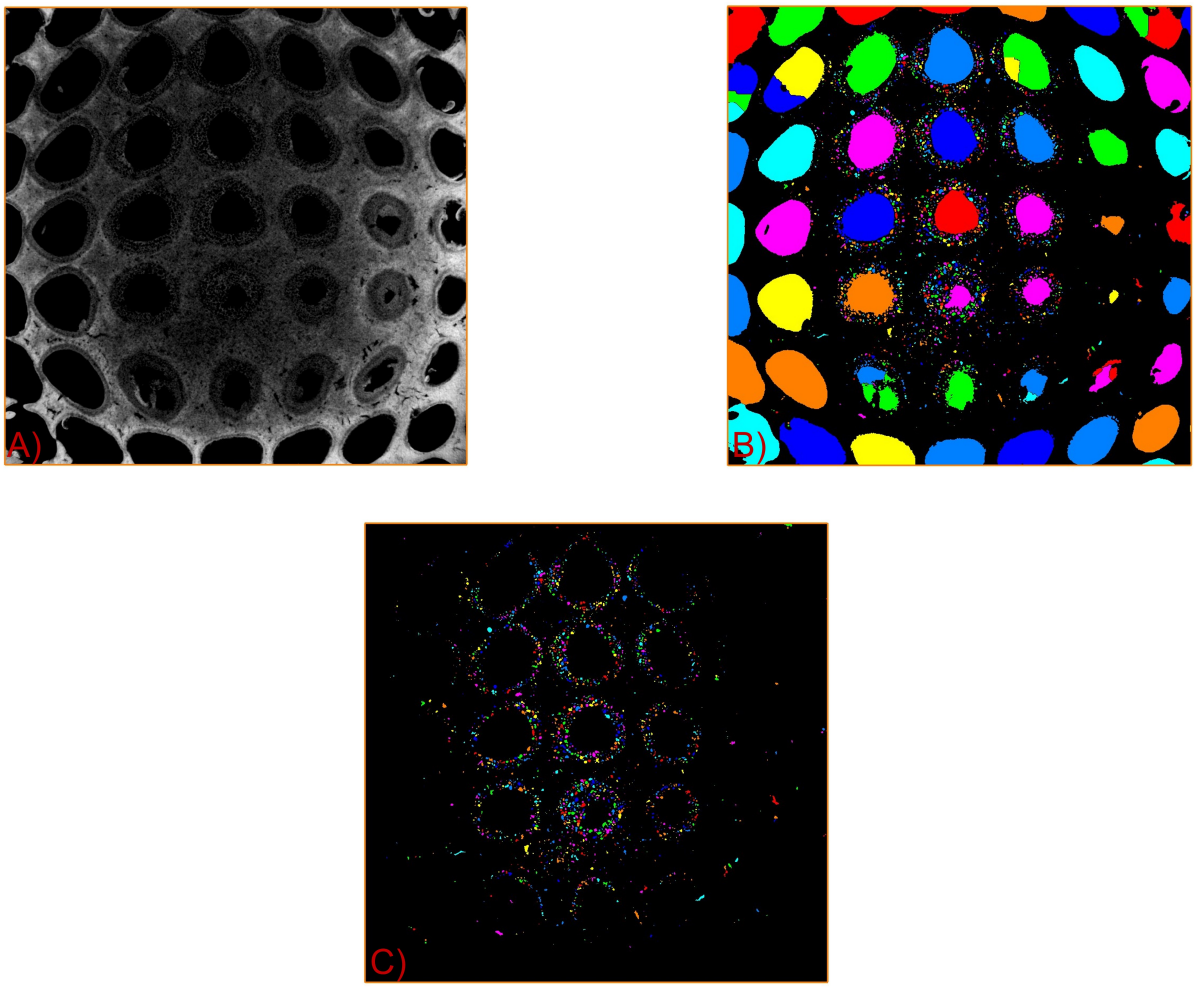

Figure 5.12: Orthogonal slice in XY-direction for CAD6; A) CT image, B) binarization of solid- and void-phase, separation and labeling of each isolated pore and C) filtering of labeled pores for pores $<0.5\text{mm}^3$.

In Figure 5.12B), it illustrates how the image-based analysis may treat some pores as two or more separate pores instead of one. This contributes to the low number of pores with a EqD above 1 mm. The grid of bigger pores are the intended pore structure, however many smaller pores can also be observed along the pore surfaces, walls and struts. In 5.12C), the separated pores are filtered. A significant amount of the small pores are concentrated in rings around bigger pore volumes. These micro pores can be caused by slurry build-up; the slurry might be partially cured because of light scattering, or it might be caused by low flowability of the resin. Even with cleaning to remove uncured resin, a majority of the glass particles will still remain inside the pore structure, resulting in a less dense glass layer after firing. This slurry residue does not only reduce the pore size, it will also prohibit interconnection in the pores. This slurry build-up is prevalent in all samples, as can be seen in Figure 5.7, but might be more prevalent in samples with smaller pore sizes. The CAD files roughly have the same porosity and the samples with a smaller pore size will inherently have a greater pore surface area in each layer for the slurry to adhere to. This might help explain the loss of porosity for CAD4 - and to a lesser degree, the other samples. However it is an inherent defect of the MSLA process, especially if the process is slurry-based [18, 17].

5.3.3 Pore connectivity

The CAD files have a completely connected pore structure in order to allow for forced convection through the pores. However, the decrease in porosity and pore size after firing might have influenced the degree of interconnection. With the image-based analysis an axis connectivity analysis was carried out. Pores not connected to the pore network will then be excluded from the porosity, allowing for investigation and visualization of the pore network. The total and connected image-based porosityi shown in Figure 5.13:

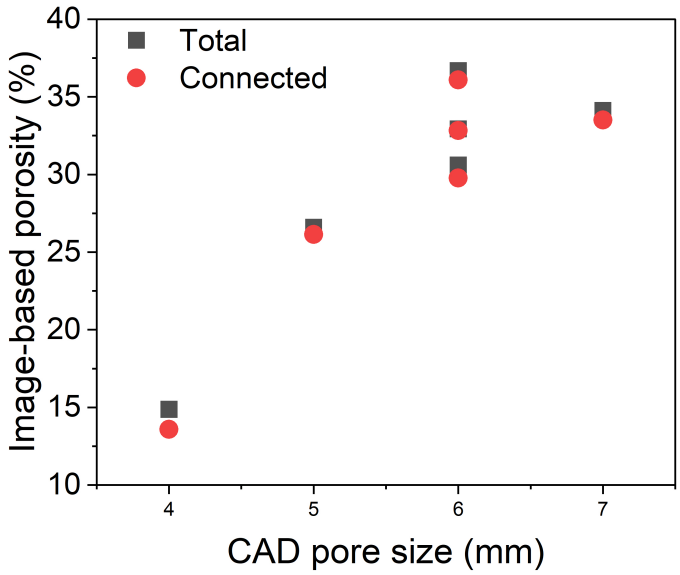

Figure 5.13: Image-based analysis and axis connectivity analysis; total and connected porosity for all samples.

The connective porosity is only slightly smaller than the total porosity, indicating that most pores are in some way connected to other pores. The high connected porosity further illustrates how the image-based analysis may be unable to detect all the sub-millimeter pores formed during debinding and sintering. These pores appear in the pore walls and struts and in the slurry build-up along the surface of bigger pores, and most will not be connected to the major pore network.

The high degree of interconnection detected with the image-based analysis is in contrast to open and closed porosities reported in Table 5.2, where most samples have a high amount of closed porosity. Determination of the open and closed porosity is done with a fluid displacement method, based on the fluid's ability to penetrate into the open and connected pores. Li et al. [56] investigated the sintering mechanism of zirconia ceramics produced with AM, and reported an asynchronous densification phenomenon during sintering. Rapid densification took place at the ceramic surface while the bulk remained under-densified. In a porous structure, this might lead the closing of the outer layer of pores, resulting in poor fluid penetration and subsequently a poor detection of the actual degree of open porosity.

Figure 5.14 shows 2D slices of all three planes of CAD5, where images containing the connected pores is subtracted from the images containing the total pore structure, resulting in images only displaying the unconnected pores.

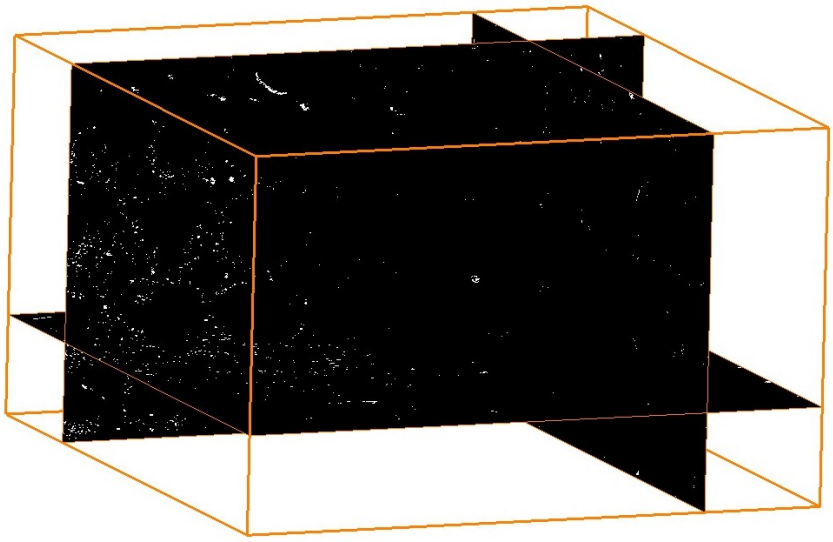

Figure 5.14: Orthogonal slices in XY-, XZ- and YZ-directions of CAD5; unconnected pores.

It is evident that the unconnected pores are mainly small and dispersed in the pore walls and struts; however, some pores are larger and resemble bigger cracks. It confirms that the macropores are in some way connected.

Pore network modeling

In order to study the characteristics of the internal pore structure more precisely, the image-based analysis allows extraction of a pore network model based on the axis connectivity analysis investigating the connectivity of the pore structure. The internal structure is visualized with spheres representing the pore and cylinders represent the internal throat, as shown in Figure 5.15:

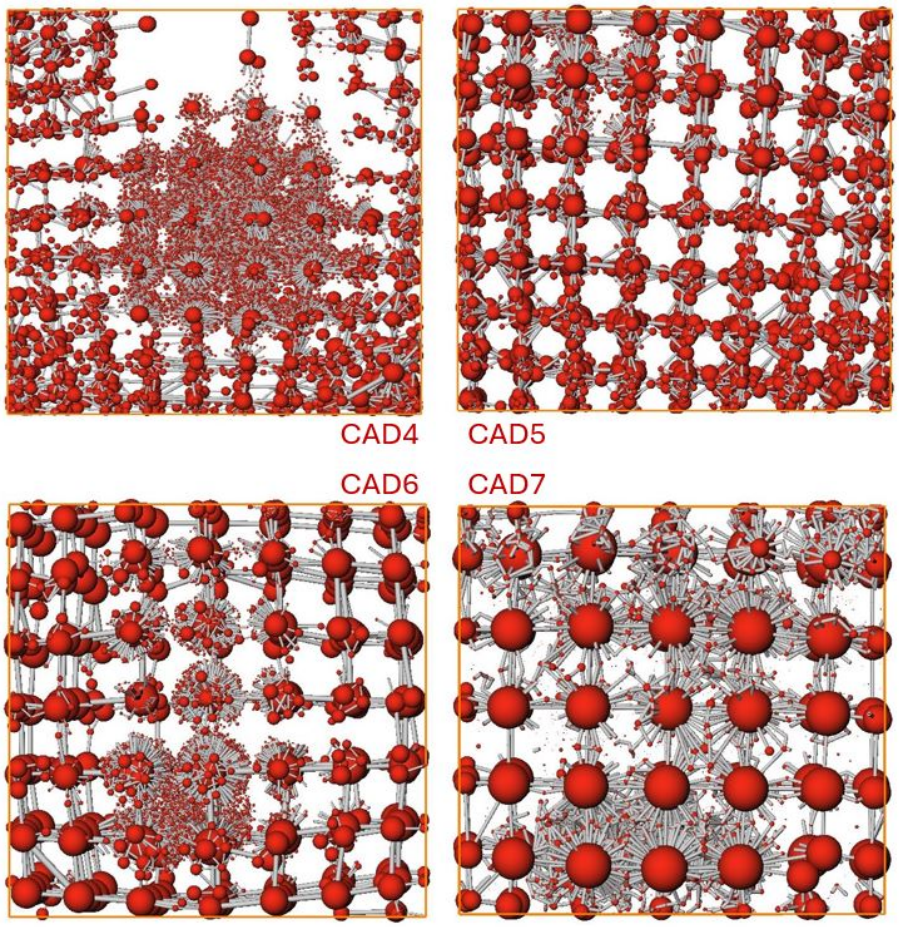

Figure 5.15: Pore network model as seen from the top of CAD4-CAD7. Spheres represent pores and cylinders represent throats.

Both the size of the sphere and the cylinder represents of the actual size of the pores and throats. Most noticeable for the pore network models is the clear grid structure which characterizes the initial CAD files. The cylinders connecting the macro pores can be seen to be similar in size to those connecting the micro pores to the pore network, suggesting small interconnections between the macro pores. All samples experience interconnection with smaller pores, however the distribution differs. CAD4 is the only sample visibly missing a part of the macro pore structure in the pore network, displaying how some macropores are completely isolated from the pore network, likely resulting in the larger difference in total and connected image-based porosity. Additionally, the center of the network is dominated by smaller pores originating from the firing process. In CAD5, it becomes harder to distinguish which pore might have originated from the CAD file and which were formed during manufacturing. It seems this sample has larger pores in the walls and struts than any other sample. Similar to CAD4, CAD6 experiences pore formation mainly in the center of the sample, distorting the grid structure of the macro pores. CAD7 exhibits micro pores throughout the structure and they are significantly smaller than the macro pores.

Interconnection is a requirement for inclusion in the pore network model. Therefore the model will not show any isolated pores. The small pores included in the network might then be pores which have coalesced or cracks connected to the big pores [18]. Some pores may have been left out of the network,

if their connection is below the resolution threshold [53]. In this regard, the pore network model will be less accurate, it does however suggest a pore structure interconnected enough to allow for convection through the pore structure.

5.4 Thermal conductivity

Porous glass structures, such as foams, are used as thermal insolation material. Understanding the thermal properties of both the the total material as well as the individual contributions is important. The image-based analysis allows for simulation of the k_{eff} and provides an k_{eff} value and a visualization of the thermal front moving through the porous material, as seen in Figure 5.16:

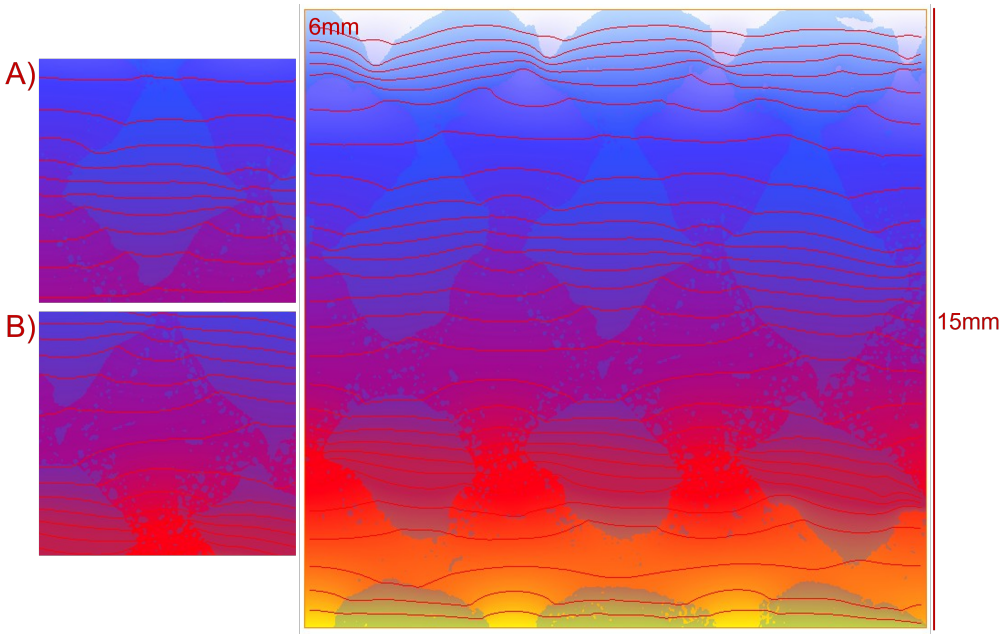

Figure 5.16: Visualization of temperature field in image-based thermal conductivity simulation. Thermal flux in Z-direction, heat input from the bottom (yellow) towards the top (light blue). A) Heat front moving through pore. B) Heat front moving through solid pore strut.

There is a decrease in temperature from the input of the sample region of interest (yellow) to the output (light blue). The red lines represent the heat fronts per time unit. The fronts move faster through the solid phase than in the gas phase, as seen in A) and B), visualizing how introducing pores into a material will decrease k_{eff} [9, 6]. The simulation relies on accurate k_{eff} values for both the solid and gas phases. The gas phase consists entirely of air, while the solid phase is assumed to be exclusively made up of CRT panel glass. It is theorized that some binder residue could be left in the solid phase impacting the actual solid conduction. However, the simulation might also be useful in predicting trends across pore sizes or porosities. Figure 5.17 and 5.18 display both simulated and experimentally determined k_{eff}, and discrepancies do exist between the simulated and measured values; for both the image-based and the gravimetric porosity the simulated data consistently over-predict the measured values across the full range of porosity. This is most likely a result of inaccurate simulation parameters, such as k_{solid} or an inaccurate quantification of the pore structure.

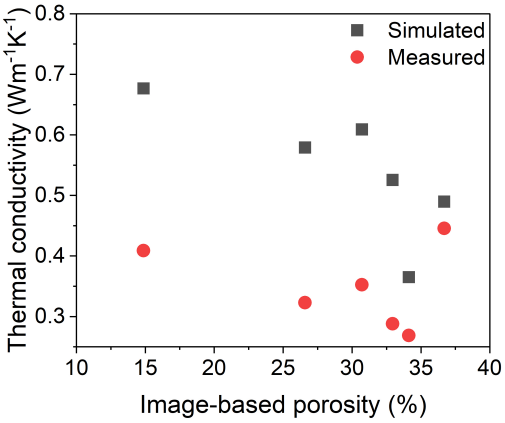

Figure 5.17: Effective thermal conductivity as a function of image-based porosity.

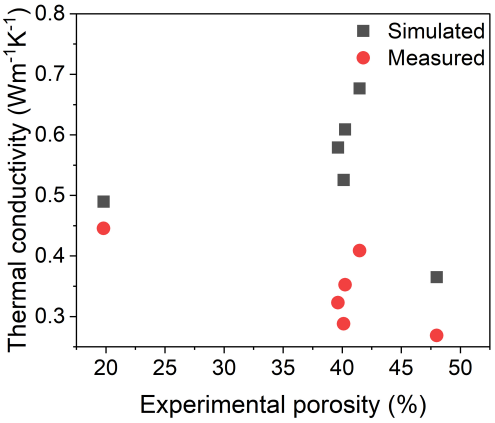

Figure 5.18: Effective thermal conductivity as a function of gravimetric porosity.

Generally, a trend of decreasing k_{eff} with increasing porosity can be observed, which is consistent with the expectation that increased pore volume reduces effective heat conduction within the whole material. A general trend of decreasing k_{eff} with increasing porosity is observed, aligning with the understanding that larger pore volumes hinder heat transfer through a material. In the case of foam glasses, the linear relationship between density, and hence porosity, and k_{eff} is well-known. Both Petersen et al. [57] and König et al. [58] reported a linear correlation between density and k_{eff}. König, using CRT panel glass to fabricate foam glass, achieved a minimum k_{eff} of $0.042\mathrm{Wm^{-1}K^{-1}}$. However, the porosities of these foams were substantially higher than those achieved for any of the samples, potentially explaining the lower k_{eff}. In contrast, Zhou et al. [59] synthesized porous glass-ceramic structures with a porosity of 50.1%, achieving a k_{eff} of $0.74\mathrm{Wm^{-1}K^{-1}}$, which is more comparable to the values observed in the present samples. The relatively higher k_{eff} of the glass-ceramics is attributed to the inherently more crystalline structure of glass-ceramics compared to amorphous glasses, which enhances thermal conduction. Consequently, despite having similar or even higher porosities, glass-ceramics tend to exhibit lower insulating performance than purely glass-based structures. This trend is further supported by Smith et al. [60], who examined hydroxyapatite ceramics and found that increasing densification from 40% to full density led to a significant rise in k_{eff}, from $0.25\mathrm{Wm^{-1}K^{-1}}$ to $1.5\mathrm{Wm^{-1}K^{-1}}$. Their findings underscore the strong influence of porosity on thermal transport properties.

In Figure 5.17 both simulated and measured data show a linear decrease with increasing porosity, but above $\sim$30% a concentration of similar porosities with varying corresponding k_{eff} appears. This behavior may suggest limitations in the image-based analysis when determining porosity at higher levels, potentially due to challenges in accurately capturing finer structural features. In Figure 5.18 an increase in the gravimetric porosity similarly decreases k_{eff}. However, at $\sim$40% porosity, this trend is less pronounced. At seemingly the same porosity k_{eff} varies with $\sim 0.1\mathrm{Wm^{-1}K^{-1}}$. These observations imply that porosity alone may not fully account for the changes in k_{eff} in the samples. In Table 5.1 the CAD porosity does not change significantly with an increase in pore size, and the same trend can generally be seen in the gravimetric porosity. However, each sample has significantly different k_{eff}, both simulated and measured. In Figure 5.19 k_{eff} can be seen as a function of CAD pore size:

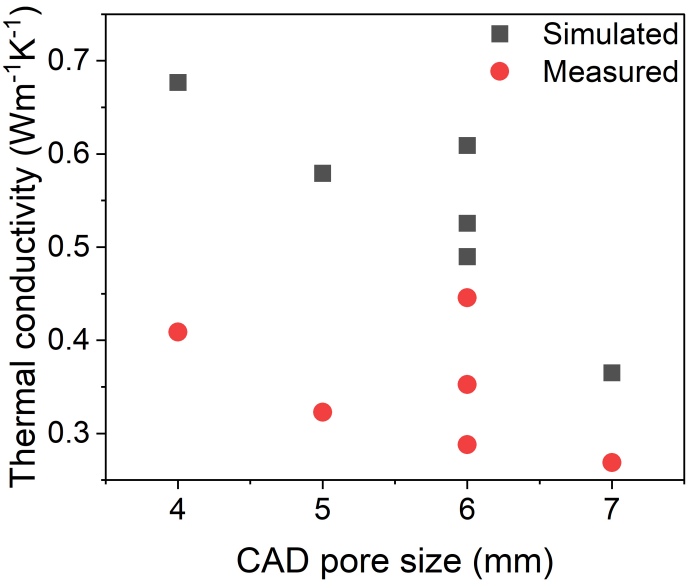

Figure 5.19: Thermal conductivity as a function of CAD pore size.

Here a similar linearity can be seen - increasing the pore size will decrease k_{eff}. Taken together, these results indicate that while porosity plays an important role, additional structural characteristics, such as pore geometry, distribution, or connectivity, may also significantly influence k_{eff} in the porous materials. However, CAD6, F1CAD6 and F2CAD6 still exhibit very different values for k_{eff}. The lowest gravimetric porosity is attributed to F1CAD6, which simultaneously is the sample with the highest image-based porosity, as can be seen in Table 5.3:

Table 5.3: Measured k_{eff}, gravimetric porosity and image-based porosity for CAD6, F1CAD6 and F2CAD6.

	CAD6	F1CAD6	F2CAD6
Measured k_{eff} ($\mathrm{Wm^{-1}K^{-1}}$)	0.35	0.45	0.29
Gravimetric porosity (%)	40.2	19.8	40.1
Image-based porosity (%)	30.7	36.6	32.9

All this further highlights how a better understanding of the relationship between k_{eff} and pore structure, size and distribution is important. The porosity of a porous material is not always enough to predict the thermal properties [9, 5].

5.4.1 Forced convection

In order to investigate the convective contribution to k_{eff}, it was measured while being subjected to a forced gas flow. The samples were placed in a cell allowing only for uniaxial flow through the sample. In order to properly gauge the influence of the flow, different rates was utilized, which can be seen in Figure 5.20:

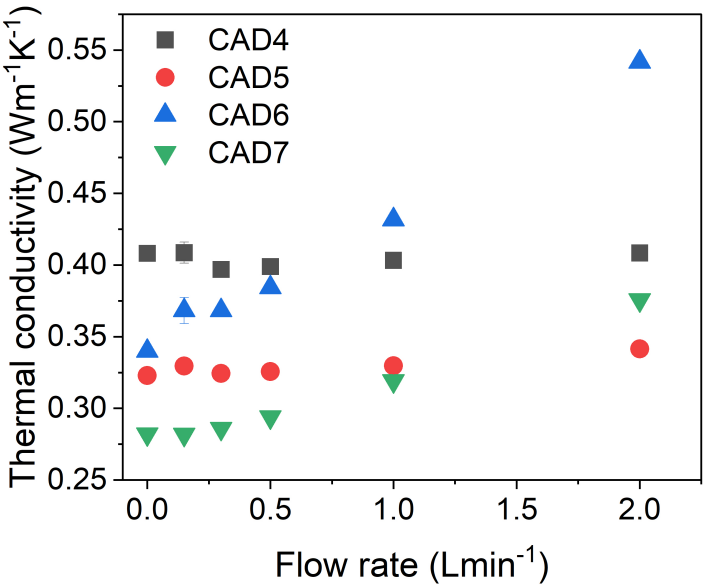

Figure 5.20: Effective thermal conductivity of CAD4-CAD7 under forced convection with flow rates in the range of $0\,\mathrm{Lmin}^{-1}$-$2\,\mathrm{Lmin}^{-1}$

k_{eff} of both CAD4 and CAD5 exhibit little to no significant increase when being subjected to increasing flow rates. There is some scatter in the data, which suggests some possible uncertainties in the data, such as sample variation or minor flow instabilities. The samples mainly exhibit pores with EqD <2-3 mm and the image-based analysis predicts a connected porosity of ~90-100% of the total porosity. The two samples additionally experienced deformation and significant pore formation during printing, debinding and sintering, which may have affected the nature of the pore structure. Small pores and limited connectivity hinder the forced convection, which might explain why forced convection has a limited affect on k_{eff}. This further supports, why the influence of convection in porous structures with small and closed pores is neglected [34, 5].

On the other hand, both CAD6 and CAD7 experience a significant increase in k_{eff} with increasing flow rate. CAD6 experiences the biggest increase in k_{eff} of $0.2\mathrm{Wm}^{-1}\mathrm{K}^{-1}$, while CAD7 only increases with $0{,}093\,\mathrm{Wm}^{-1}\mathrm{K}^{-1}$. The steep rate of change in k_{eff} for CAD6 suggests that the sample has the most connected pore network, but it might also have a more directionally aligned structure, which supports uniaxial convection more efficiently than CAD7. In Table 5.1 CAD7 can be seen to have a greater image-based and gravimetric porosity, as well as having larger macro pores compared to CAD6. All this will make k_{eff} for CAD7 lower, which is also reflected in Figure 5.20. All this illustrates the complex connection between pore structure and convective heat transfer in porous materials. While CAD4 and CAD5 display minimal sensitivity to forced convection due to their small, poorly connected pores, CAD6 and CAD7 demonstrate clear increases in k_{eff} with gas flow, highlighting the importance of pore connectivity and size. Notably, the stronger response in CAD6 compared to CAD7 suggests that not only the presence but also the arrangement and scale of pores play a critical role in enabling convective contributions. Overall, the results emphasize that k_{eff} under forced convection is not easily predicted by porosity alone, but must also account for structural factors such as pore morphology, connectivity, and

distribution.

6 | Conclusion

Additive manufacturing has demonstrated strong potential as a fabrication method for porous glass structures. In this work, masked stereolithography was employed to produce such structures using CRT glass particle at a 50 wt.% loading, with designed pore sizes ranging from 2-7mm. X-ray tomography allows for a non-destructive characterization of the internal pore structure post manufacturing, and confirmed successful fabrication of the intended macro-porous geometry. However, tomography also reveal some deformation of the pore structure; build-up of slurry on the internal pore surface, which reduces the pore sizes and blocks the interconnected structure of the pores, crack formation along the print orientation and pore formation in the pore walls and struts.

It is found, that both the gravimetric and image-based porosity is reduced compared to the designed porosity, however it is an inherent result of shrinkage caused by particle sintering and possible deformation. The image-based analysis further demonstrated that, despite the presence of sub millimeter pores formed during firing, the designed macro pores dominated the overall pore volume. The volume of the pores for all six samples is found to be broadly distributed, illuminating how shrinkage and slurry build-up can happen anisotopically in the samples.

Image-based modeling of the pore network reveals that the connected porosity is nearly equal to the total image-based porosity, suggesting that macro pores maintains connectivity despite deformation. Visualization of the unconnected pores located them primarily in the pore walls and struts, indicating that the macro pores stays connected despite deformation. Gravimetric porosity measurements also enables assessment of the open vs. closed pore fractions, and shows a >95% closed porosity for almost all samples. However, high surface densification may compromise the reliability of the fluid displacement method, as surface-closed porosity could be obscuring detection of the internal open network.

Image-based analysis enables simulations of the thermal conductivity, and the attained results show a decreased on conductivity with an increased pore size, consistent with experimental measurements. Similar porosities across all samples makes it difficult to gauge the influence of pore structure on the thermal conductivity, however the designed pore sizes highlights the influence of pore sizes and porosity on the thermal transport properties.

Finally, the interconnected nature determined with the image-based analysis is a prerequisite for determining the effect of forced convection on the thermal conductivity. While CAD4 and CAD exhibited no significant change, samples CAD6 and CAD7 showed increased conductivity under forced convection, especially at higher flow rates. For CAD6 a flow rate of $2\mathrm{Lmin}^{-1}$ increased the thermal conductivity with $\sim 0.1\mathrm{Wm}^{-1}\mathrm{K}^{-1}$.

Bibliography

[1] D. K. Hale. The physical properties of composite materials. *Journal of Materials Science*, 11(11):2105–2141, November 1976.

[2] Terry M. Tritt. *Thermal conductivity; Theory, Properties and Application*. Kluwer Academic/Plenum Publishers, 2004.

[3] Eric S. Toberer, Lauryn L. Baranowski, and Chris Dames. Advances in thermal conductivity. *Annual Review of Materials Research*, 42(Volume 42, 2012):179–209, 2012.

[4] He Liu and Xinpeng Zhao. Thermal conductivity analysis of high porosity structures with open and closed pores. *International Journal of Heat and Mass Transfer*, 183:122089, 2022.

[5] Jakob König, Vincenc Nemanič, Marko Žumer, Rasmus R. Petersen, Martin B. Østergaard, Yuanzheng Yue, and Danilo Suvorov. Evaluation of the contributions to the effective thermal conductivity of an open-porous-type foamed glass. *Construction and Building Materials*, 214:337–343, 2019.

[6] Minggang Luo, Cuilin Wang, Junming Zhao, and Linhua Liu. Characteristics of effective thermal conductivity of porous materials considering thermal radiation: A pore-level analysis. *International Journal of Heat and Mass Transfer*, 188:122597, 2022.

[7] David S. Smith, Arnaud Alzina, Julie Bourret, Benoît Nait-Ali, Fabienne Pennec, Nicolas Tessier-Doyen, Kodai Otsu, Hideaki Matsubara, Pierre Elser, and Urs T. Gonzenbach. Thermal conductivity of porous materials. *Journal of Materials Research*, 28(17):2260–2272, July 2013.

[8] Miguel A.A. Mendes, Prabal Talukdar, Subhashis Ray, and Dimosthenis Trimis. Detailed and simplified models for evaluation of effective thermal conductivity of open-cell porous foams at high temperatures in presence of thermal radiation. *International Journal of Heat and Mass Transfer*, 68:612–624, 2014.

[9] Martin B. Østergaard, Biao Cai, Rasmus R. Petersen, Jakob König, Peter D. Lee, and Yuanzheng Yue. Impact of pore structure on the thermal conductivity of glass foams. *Materials Letters*, 250:72–74, 2019.

[10] Martin B. Østergaard, Rasmus R. Petersen, Jakob König, Hicham Johra, and Yuanzheng Yue. Influence of foaming agents on solid thermal conductivity of foam glasses prepared from crt panel glass. *Journal of Non-Crystalline Solids*, 465:59–64, 2017.

[11] Zhangwei Chen, Ziyong Li, Junjie Li, Chengbo Liu, Changshi Lao, Yuelong Fu, Changyong Liu, Yang Li, Pei Wang, and Yi He. 3d printing of ceramics: A review. *Journal of the European Ceramic Society*, 39(4):661–687, 2019.

[12] Ian Gibson, David Rosen, Brent Stucker, and Mahyar Khorasani. *Additive manufacturing technologies : [hbk.]*. Springer, Cham, third edition edition, 2021.

[13] Tuan D. Ngo, Alireza Kashani, Gabriele Imbalzano, Kate T.Q. Nguyen, and David Hui. Additive manufacturing (3d printing): A review of materials, methods, applications and challenges. *Composites Part B: Engineering*, 143:172–196, 2018.

[14] Chenxing Xin, Zheng Li, Liang Hao, and Yan Li. A comprehensive review on additive manufacturing of glass: Recent progress and future outlook. *Materials & Design*, 227:111736, 2023.

[15] Kuan-Yu Chiu, Chih-Ling Huang, Jian-Yuan Huang, Tzer-Min Lee, Guo-Chung Dong, Ker-Kong Chen, and Yan-Hsiung Wang. Fabrication of bioactive glass scaffolds by stereolithography: Influence of particle size and surfactant concentration. *Ceramics International*, 49(10):15295–15303, 2023.

[16] Faqiang Zhang, Jingzhou Yang, Yangbo Zuo, Kaixin Li, Zhe Mao, Xia Jin, Shupei Zhang, Hairui Gao, and Yingqiu Cui. Digital light processing of beta-tricalcium phosphate bioceramic scaffolds with controllable porous structures for patient specific craniomaxillofacial bone reconstruction. *Materials & Design*, 216:110558, 2022.

[17] Keqiang Zhang, Qiaoyu Meng, Zhaoliang Qu, and Rujie He. A review of defects in vat photopolymerization additive-manufactured ceramics: Characterization, control, and challenges. *Journal of the European Ceramic Society*, 44(3):1361–1384, 2024.

[18] Xiangquan Wu, Jiachen Teng, Xiangxu Ji, Chunjie Xu, Dong Ma, Shang Sui, and Zhongming Zhang. Research progress of the defects and innovations of ceramic vat photopolymerization. *Additive Manufacturing*, 65:103441, 2023.

[19] Xiangquan Wu, Chunjie Xu, and Zhongming Zhang. Preparation and optimization of si3n4 ceramic slurry for low-cost lcd mask stereolithography. *Ceramics International*, 47(7, Part A):9400–9408, 2021.

[20] Jiaxian Fan, Xiqing Xu, Shuxin Niu, Yulong Zhou, Xin Li, Yajie Guo, and Yushi Luo. Anisotropy management on microstructure and mechanical property in 3d printing of silica-based ceramic cores. *Journal of the European Ceramic Society*, 42(10):4388–4395, 2022.

[21] E. Schwarzer, M. Götz, D. Markova, D. Stafford, U. Scheithauer, and T. Moritz. Lithography-based ceramic manufacturing (lcm) – viscosity and cleaning as two quality influencing steps in the process chain of printing green parts. *Journal of the European Ceramic Society*, 37(16):5329–5338, 2017. Shaping of Advanced Ceramics.

[22] Chuchu Qian, Kehui Hu, Junhua Li, Peijie Li, and Zhigang Lu. The effect of light scattering in stereolithography ceramic manufacturing. *Journal of the European Ceramic Society*, 41(14):7141–7154, 2021.

[23] Gerald Mitteramskogler, Robert Gmeiner, Ruth Felzmann, Simon Gruber, Christoph Hofstetter, Jürgen Stampfl, Jörg Ebert, Wolfgang Wachter, and Jürgen Laubersheimer. Light curing strategies

for lithography-based additive manufacturing of customized ceramics. *Additive Manufacturing*, 1-4:110–118, 2014. Inaugural Issue.

[24] Qin Lian, Xiangquan Wu, Dichen Li, Xiaoning He, Jiali Meng, Xiaodong Liu, and Zhongmin Jin. Accurate printing of a zirconia molar crown bridge using three-part auxiliary supports and ceramic mask projection stereolithography. *Ceramics International*, 45(15):18814–18822, 2019.

[25] Chongyu Long, Long Jiang, Shufeng Xiong, Zhiyuan Liu, Changyong Liu, and Zhangwei Chen. Effective post-cleaning strategy for vat photopolymerization 3d printed complex-structured polymer-derived ceramics. *Additive Manufacturing*, 94:104456, 2024.

[26] Jason C. Young, Stephan A. Brinckmann, Andrew Fox, Ray S. Fertig, Stephen P. Lynch, and Carl P. Frick. On enhancing the manufacturability and conversion of additively manufactured polymer-derived ceramics. *Journal of the European Ceramic Society*, 44(14):116691, 2024.

[27] He Li, Yongsheng Liu, Yansong Liu, Kehui Hu, Zhigang Lu, and Jingjing Liang. Investigating the relation between debinding atmosphere and mechanical properties of stereolithography-based three-dimensional printed al2o3 ceramic. *Proceedings of the Institution of Mechanical Engineers, Part B: Journal of Engineering Manufacture*, 234(14):1686–1694, July 2020.

[28] He Li, Yongsheng Liu, Yansong Liu, Qingfeng Zeng, Kehui Hu, Zhigang Lu, and Jingjing Liang. Effect of debinding temperature under an argon atmosphere on the microstructure and properties of 3d-printed alumina ceramics. *Materials Characterization*, 168:110548, 2020.

[29] Guang-Xin Mao, Jia-Min Wu, Chong Tian, Chun-Lei Liu, Xin Lin, Fen Wang, Hai-Sheng Xu, and Yu-Sheng Shi. Improved mechanical properties of porous si3n4 ceramics strengthened by beta-si3n4 seeds fabricated by vat photopolymerization. *Ceramics International*, 50(23, Part A):49058–49065, 2024.

[30] Anna-Katharina Hofer, Andraž Kocjan, and Raúl Bermejo. High-strength lithography-based additive manufacturing of ceramic components with rapid sintering. *Additive Manufacturing*, 59:103141, 2022.

[31] He Li, Yongsheng Liu, Paolo Colombo, Wenbo Li, Yansong Liu, Kehui Hu, and Zhigang Lu. The influence of sintering procedure and porosity on the properties of 3d printed alumina ceramic cores. *Ceramics International*, 47(19):27668–27676, 2021.

[32] Charles Manière, Gabriel Kerbart, Christelle Harnois, and Sylvain Marinel. Modeling sintering anisotropy in ceramic stereolithography of silica. *Acta Materialia*, 182:163–171, January 2020.

[33] Farnaz Batool, Muhammad Masood Rafi, and Vivek Bindiganavile. Microstructure and thermal conductivity of cement-based foam:a review. *Journal of Building Engineering*, 20:696–704, 2018.

[34] Erdem Cuce, Pinar Mert Cuce, Christopher J. Wood, and Saffa B. Riffat. Toward aerogel based thermal superinsulation in buildings: A comprehensive review. *Renewable and Sustainable Energy Reviews*, 34:273–299, 2014.

[35] C.Y. Zhao. Review on thermal transport in high porosity cellular metal foams with open cells. *International Journal of Heat and Mass Transfer*, 55(13):3618–3632, 2012.

[36] Micheal Scheffer and Paolo Colombo. *Cellular Ceramics; Structure, manufacturing, properties and applications*. WILEY-VCH verlag GmbH & Co. KGaA, Weinheim, 2005.

[37] Christine B. Pedersen, Morten Haunsvig, and Jakob K. Mikkelsen. *Fabrication of Porous CRT Panel Glass Structures with MSLA: Sedimentation Influences, 3D-Printer Settings and Sintering Parameters*, 2024. Semester Project, AAU.

[38] Zhanwen Xing, Hongzhi Zhou, Weiwei Liu, Jianbin Nie, Yao Chen, and Wenli Li. Efficient cleaning of ceramic green bodies with complex architectures fabricated by stereolithography-based additive manufacturing via high viscoelastic paste. *Additive Manufacturing*, 55:102809, 2022.

[39] George Wypych. Phema poly(2-hydroxyethyl methacrylate). In George Wypych, editor, *Handbook of Polymers*, pages 410–411. Elsevier, Oxford, 2012.

[40] chemspider.com. Trimethylolpropane triacrylate. `http://www.chemspider.com/Chemical-Structure.25519.html` [Accessed: 02/06/2025].

[41] chembk.com. Photoinitiator-819. `https://www.chembk.com/en/chem/Photoinitiator-819` [Accessed: 02/06/2025].

[42] Hugo R. Fernandes, Fernanda Andreola, Luisa Barbieri, Isabella Lancellotti, Maria J. Pascual, and José M.F. Ferreira. The use of egg shells to produce cathode ray tube (crt) glass foams. *Ceramics International*, 39(8):9071–9078, 2013.

[43] James E. Shelby and Maria Lopes. *Introduction to Glass Science and Technology*. The Royal Society of Chemistry, 2005.

[44] Mettler Toledo. Density kit. for solids and liquids determination. `www.mt.com`, 2010. (Handout from supervisor).

[45] Rasmus Rosenlund Petersen, Jakob König, Morten Mattrup Smedskjær, and Yuanzheng Yue. Foaming of crt panel glass powder using na_2co_3. *Glass Technology: European Journal of Glass Science and Technology Part A*, 55(1):1–6, February 2014.

[46] Sandeep Kumar Paral, Ding-Zheng Lin, Yih-Lin Cheng, Shang-Chih Lin, and Jeng-Ywan Jeng. A review of critical issues in high-speed vat photopolymerization. *Polymers*, 15(12):2716, June 2023.

[47] Yayue Pan, Haiyang He, Jie Xu, and Alan Feinerman. Study of separation force in constrained surface projection stereolithography. *Rapid Prototyping Journal*, 23(2):353–361, March 2017.

[48] Andrea Zocca, Paolo Colombo, Cynthia M. Gomes, and Jens Günster. Additive manufacturing of ceramics: Issues, potentialities, and opportunities. *Journal of the American Ceramic Society*, 98(7):1983–2001, July 2015.

[49] Keqiang Zhang, Chen Xie, Gang Wang, Rujie He, Guojiao Ding, Min Wang, Dawei Dai, and Daining Fang. High solid loading, low viscosity photosensitive al2o3 slurry for stereolithography based additive manufacturing. *Ceramics International*, 45(1):203–208, 2019.

[50] Thermo Fisher Scientific. *Avizo Software User's Guide*. Thermo Fisher Scientific, 2019. Version 2019.

[51] Nan Fan, Jiren Wang, Cunbao Deng, Yongpeng Fan, Tingting Wang, and Xiaoyang Guo. Quantitative characterization of coal microstructure and visualization seepage of macropores using ct-based 3d reconstruction. *Journal of Natural Gas Science and Engineering*, 81:103384, 2020.

[52] Bartłomiej Gackiewicz, Krzysztof Lamorski, and Cezary Sławiński. Saturated water conductivity estimation based on x-ray ct images – evaluation of the impact of thresholding errors. *International Agrophysics*, 33(1):49–60, February 2019.

[53] V. Cnudde and M.N. Boone. High-resolution x-ray computed tomography in geosciences: A review of the current technology and applications. *Earth-Science Reviews*, 123:1–17, 2013.

[54] Peter Evans, Griffin Turner, Raj Patel, Mohammadamin Moghadasi, Qirong Yang, Zhijian Pei, Chao Ma, James D. Paramore, Brady G. Butler, and Kelvin Y. Xie. Shrinkage, microstructure, and mechanical properties of sintered 3d-printed silica via stereolithography. *International Journal of Applied Ceramic Technology*, 21(3):1638–1647, November 2023.

[55] Seyed Mohammad Sajadi, Lívia Vásárhelyi, Reza Mousavi, Amir Hossein Rahmati, Zoltán Kónya, Ákos Kukovecz, Taib Arif, Tobin Filleter, Robert Vajtai, Peter Boul, Zhenqian Pang, Teng Li, Chandra Sekhar Tiwary, Muhammad M. Rahman, and Pulickel M. Ajayan. Damage-tolerant 3d-printed ceramics via conformal coating. *Science Advances*, 7(28), July 2021.

[56] Hezhen Li, Lu Song, Jialin Sun, Jing Ma, and Zhijian Shen. Asynchronous densification of zirconia ceramics formed by stereolithographic additive manufacturing. *Journal of the European Ceramic Society*, 41(8):4666–4670, 2021.

[57] Rasmus R. Petersen, Jakob König, and Yuanzheng Yue. The mechanism of foaming and thermal conductivity of glasses foamed with mno2. *Journal of Non-Crystalline Solids*, 425:74–82, 2015.

[58] Jakob König, Rasmus R. Petersen, and Yuanzheng Yue. Fabrication of highly insulating foam glass made from crt panel glass. *Ceramics International*, 41(8):9793–9800, 2015.

[59] Jian Zhou, Jinshan Lu, Changyou Liu, and Liang Chen. Preparation, pore structure and properties of uniformly porous glass-ceramics sintered from granite powder using sic@sio2 foaming agent. *Ceramics International*, 50(24, Part A):52379–52387, 2024.

[60] David S. Smith, Pierre Lefeuvre, Maxence Renaux, Benoit Nait-Ali, and Anne Leriche. Study of neck formation and densification in porous hydroxyapatite ceramics using thermal conductivity measurements. *Open Ceramics*, 13:100329, 2023.

A | X-ray tomography scanning parameters

Table A.1: X-ray tomography scanning parameters for all samples

	Voxel size (μm)	Voxel count	Distance to source (mm)
CAD4	17.26	2961 (X) 3002 (Y) 1445 (Z)	133.7
CAD5	17.57	3192 (X) 3192 (Y) 2296 (Z)	136.1
CAD6	17.54	2899 (X) 2957 (Y) 1410 (Z)	135.9
CAD7	16.42	3008 (X) 2954 (Y) 1079 (Z)	127.2
F1CAD6	17.78	2816 (X) 2940 (Y) 1415 (Z)	137.7
F2CAD6	18.67	3049 (X) 3030 (Y) 1291 (Z)	144.6

B | Gravimetric porosity

Table B.1

	CAD4	CAD5	CAD6	CAD7	F1CAD6	F2CAD2
w_{dry} (g)	31.5166	29.3022	26.0812	14.9212	29.2557	27.956
w_{water} (g)	19.426	17.5148	15.7451	10.3517	13.1608	16.8439
ρ_{foam} (gcm^{-3})	1.6195	1.6700	1.6535	1.4388	2.2189	1.6567
ρ_{skel} (gcm^{-3})	1.6481	1.7877	1.6844	1.7399	2.5436	1.6773

C | Thermal conductivity simulation

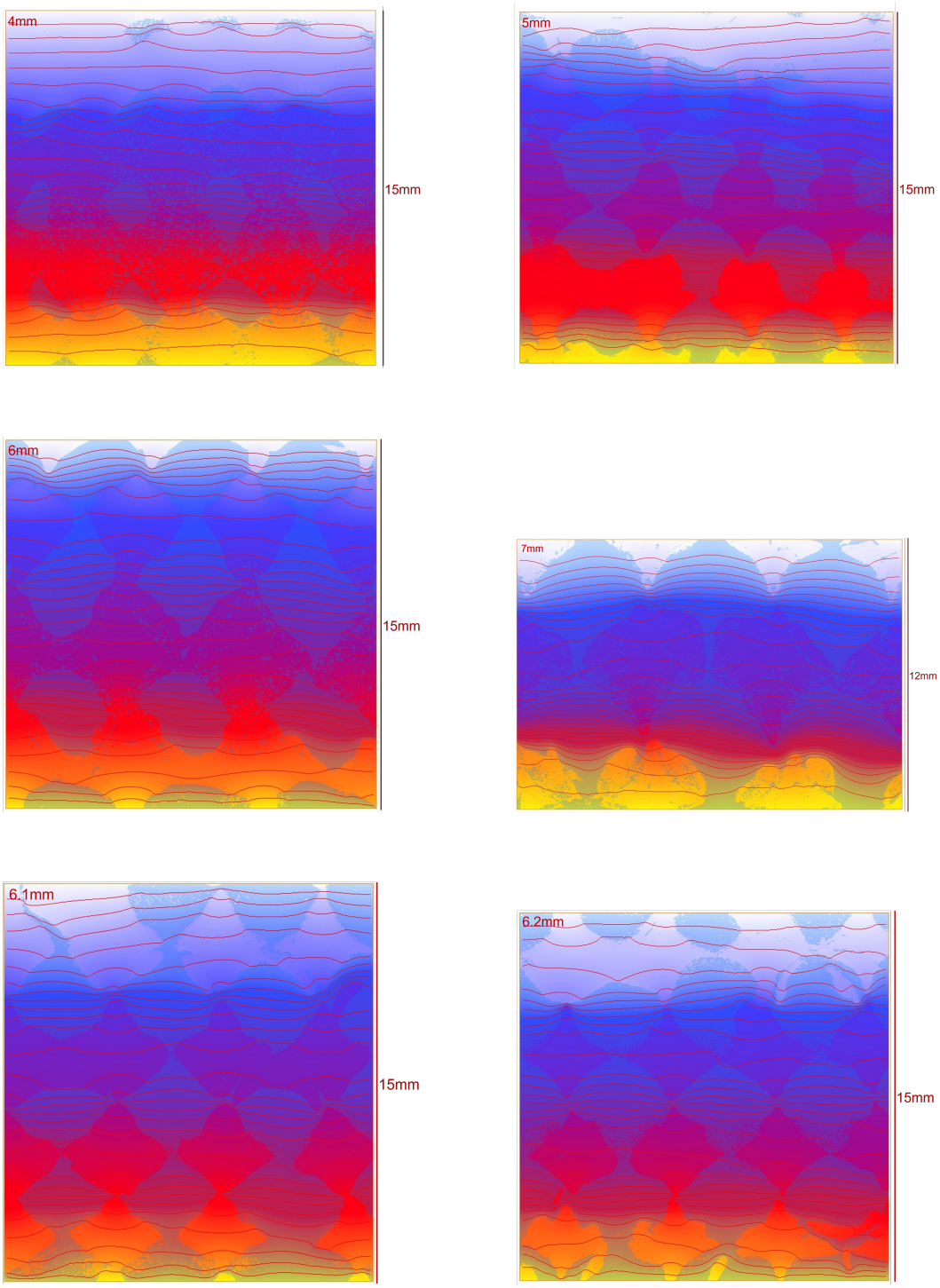

Figure C.1: Full page collection of figures